Photonics in switching: enabling technologies and subsystem design

Kyriakos Vlachos,[1,*] Carla Raffaelli,[2] Slavisa Aleksic,[3] Nicola Andriolli,[4] Dimitris Apostolopoulos,[5] Hercules Avramopoulos,[5] Didier Erasme,[6] Dimitris Klonidis,[7] Martin Nordal Petersen,[8] Mirco Scaffardi,[4] Karsten Schulze,[9] Maria Spiropoulou,[7] Stelios Sygletos,[10] Ioannis Tomkos,[7] Carmen Vazquez,[11] Olga Zouraraki,[5] and Fabio Neri[12]

[1]*Computer Engineering and Informatics Department and Research Academic Computer Technology Institute, University of Patras, Rio, Greece*
[2]*Dipartimento di Elettronica, Informatica e Sistemistica, University of Bologna, Viale Risorgimento, 2, Bologna, Italy*
[3]*Vienna University of Technology, Institute of Communication Networks, Favoritenstrasse 9/388, A-1040 Vienna, Austria*
[4]*Scuola Superiore Sant'Anna, Pisa 56124, Italy*
[5]*National Technical University of Athens, Zografou, GR 15773 Athens, Greece*
[6]*Communications and Electronics Department, Institute TELECOM, TELECOM ParisTech, Laboratoire Traitement et Communication de l'Information, CNRS, 75634 Paris Cedex 13, France*
[7]*Athens Information Technology Centre (AIT), 19002 Peania, Athens, Greece*
[8]*DTU Fotonik, Department of Photonics Engineering, Technical University of Denmark, Ørsteds Plads 343, DK-2800 Kgs. Lyngby, Denmark*
[9]*Universidad Politécnica de Valencia (UPVLC), Nanophotonics Technology, Center, Valencia, Spain*
[10]*Institute of High-Frequency and Quantum Electronics, University of Karlsruhe (TH), D-76131 Karlsruhe, Germany*
[11]*Electronics Technology Department, Carlos III University of Madrid, 28911 Leganés, Spain*
[12]*Dipartimento di Elettronica, Politecnico di Torino, Corso Duca degli Abruzzi, 29 — 10129, Torino, Italy*
**Corresponding author: kvlachos@ceid.upatras.gr*

Received June 25, 2008; revised October 14, 2008; accepted February 13, 2009; published April 7, 2009 (Doc. ID 97123)

This paper describes recent research activities and results in the area of photonic switching carried out within the framework of the EU-funded e-Photon/ONe+ network of excellence, Virtual Department on Optical Switching. Technology aspects of photonics in switching and, in particular, recent advances in wavelength conversion, ring resonators, and packet switching and processing subsystems are presented as the building blocks for the implementation of a high-performance router for the next-generation Internet. © 2009 Optical Society of America

OCIS codes: 060.0060, 060.1155, 060.4510.

1. Introduction

Present-day applications of the high capacity provided by optical fiber mainly concern point-to-point links, possibly equipped with amplifiers. As a consequence, optical WDM lightpaths are static and are bound to be considered as a scarce resource. Once set up, they remain in place, essentially forever. Thus, current optical networks are static wavelength (circuit) switched, where optical cross-connects (OXCs) are used to switch traffic [1]. However, optical circuit switching (OCS) perfectly fits for smooth traffic of constant bit rates, but is unsuitable for dynamical optical networking to support bursty traffic. Optical packet switching (OPS) [2] has been proposed for the on-demand use of capacity. Although very promising, this technology lags behind due to the lack of a true optical random access memory. This stresses the need for on-the-fly packet processing, which is impossible with the current state-of-the-art all-optical logic [3]. Another promising candidate is optical burst switching (OBS), which combines the merits of packet and circuit switching [4]. OBS has been proposed to relax the technology constraints of OPS by attaining the dynamic, fast setup of virtual lightpaths. In any case, it is only the switching speed that really transforms the raw

bit rates into useful bandwidth, and photonic technology plays an important role toward this aim. To support dynamic optical networking, optical routers with fast reconfiguration capability are required. In recent years many research activities have been investigating architectural solutions for optical router implementation [5–7]. A key point is the availability of feasible enabling photonic technology to meet architectural and operational requirements.

This paper reviews the state of the art of photonic technology for high-performance optical switching and reports recent research results from the Virtual Department on Optical Switching and Systems (VD-S), part of the e-Photon/ONe+ and ICT-BONE network of excellence [8,9]. Together with another paper mainly related to system aspects and experiments in photonic switching [10], it provides a quite complete overview of the current research activities in that field to offer a common knowledge platform to stimulate further research. The e-Photon/ONe+ network of excellence is an EU-funded project that aims at integrating and developing knowledge in the field of optical networking and photonic technology. The VD-S working group consists of 22 academic and industrial partners, and its scope is to identify and develop key switching technologies to make the spectrum efficient in terms of switching and not only in terms of capacity. Toward this goal, the VD-S working group developed synergies between partners through collaborative projects, including mobility actions for integrating researchers and for obtaining access to unique experimental facilities and optical test beds.

Within the course of the VD-S group, key optical subsystems that have been identified to exhibit significant performance advances over other candidate technologies are optical buffers, optical multiplexers/demultiplexers, and optical packet/burst switches. However, to achieve the advantages of high performance and low power consumption that photonics can offer, other building blocks such as wavelength converters, optical logic gates, and regenerators must be developed. This paper reviews the enabling technology, presents the recent advances in the design and development of such subsystems, and presents recent efforts toward the implementation of a true all-optical packet switching node.

The rest of the paper is organized as follows. Section 2 presents enabling optical technologies and is particularly focused on recent advances in hybrid integration, wavelength conversion, and ring resonator's capabilities. Sections 3–5 present the state of the art in these areas and research results carried out and under the organization of VD-S. Finally Section 6 concludes the paper.

2. Enabling Technologies

2.A. Hybrid Integration of Active-Passive Devices

Interferometric optical gates based on semiconductor optical amplifiers (SOAs) have emerged as main candidates for the implementation of photonic signal processing circuits, exploiting their fast response for high-speed operation [11,12]. In addition, advances in hybrid and monolithic integration techniques [13] can now offer compact switching elements. Single-element, high-speed all-optical gates have been demonstrated as integrated devices in a number of laboratories across the world [14,15] and have been developed as commercial products, primarily for wavelength conversion and regeneration purposes [16]. These devices have been employed in single-gate experiments to perform wavelength conversion at rates over 160 Gbits/s or regeneration with bitwise processing capability in excess of 40 Gbits/s. In this way they offer a viable platform for high-speed processing required by future circuit switched nodes. However, most research in wavelength conversion and regeneration configurations has been focused on continuously increasing the processing speed performance of optical gates and not on exploring their logical and functional potential.

The evolution from fiber-based single-gate experiments to more complex all-optical subsystems has been made possible due to the development of compact optical gates and flip-flops based on SOAs and Mach–Zehnder interferometers (MZIs) that exploit the integration capabilities of hybrid technology. Hybrid integration is uniquely designed for passive assembly of different components in order to maintain high optical performance and low insertion losses, but at much lower cost. With an approach similar to that of an electronic printed circuit board used in electronics, a planar silica-on-silicon waveguide acts as a motherboard to host both active and passive

devices. Integration is achieved by plugging precision-machined silicon submounts or daughterboards carrying individual optical components into the motherboard. The individual components have precision-cleaved features for accurate mechanical positioning on the daughterboard. The first milestone on the development of all-optical subsystems is reached by verifying that discrete, yet integrated and compact, all-optical gates can be interconnected to produce all-optical circuits with increased functionality and intelligence. The next milestone involves the integration of generic optical gates on the same hybrid platform, in order to reduce packaging costs and increase the photonic integration level.

Figure 1 shows photographs of photonic integrated prototype devices along with the corresponding motherboard schematic designs. The fully packaged and pigtailed SOA-MZI optical gate is shown in Fig. 1(a), along with the motherboard design, as shown in Fig. 1(b) [16]. The fiber pigtailing is also achieved with a passive assembly approach using arrays of optical fibers in precision V-grooves on a silicon carrier. The daughterboard depicted in Fig. 1(c) consists of a twin SOA array and is flip-chipped onto the motherboard. Figure 1(d) shows the photograph of a quadruple array of optical gates recently integrated using hybrid integration technology. The corresponding motherboard design is shown in Fig. 1(e) with two daughterboards clearly marked. In this case, each daughterboard hosts a quadruple array of SOAs, forming two SOA-MZI optical gates. In such cases, for the development of single-element SOA-MZI optical gates, the daughterboards are designed to host monolithic twin SOA chips and provide all suitable alignment stops. These SOAs are specially designed to have high gain and maximized nonlinearity by incorporating optical mode expanders. The mode expanders enhance the optical performance by reducing the facet reflectivity to less than 10^{-5}, which allows high gain to be maintained at high bias currents. They also facilitate passive alignment by reducing the sensitivity of the coupling loss to misalignment.

The next logical step on this migration path lies at the photonic integration level. Next-generation photonic devices must include on-chip interconnections and integration of different optical components on a single chip. These devices will pave the way toward the development of true all-optical systems-on-chip, reducing both packaging and pigtailing costs, while retaining cost-effectiveness by exploiting a unified integration platform. Toward this milestone, research has already commenced reporting devices for WDM applications containing a SOA-MZI regenerator and a passband filter [17] on a single chip. The achievable integration level at any given time will be defined through the interplay between the monolithic technology developed and the hybrid platform capabilities. Hybrid integration is used for increasing integration scale and functionality, while maintaining high yield and cost-effectiveness, through integration of passive elements, such as filters, isolators, and arrayed waveguide gratings (AWGs) onto a single platform. The advent of monolithic technology toward the development of larger monolithic chips will allow for constantly upgrading the fundamental active element of the developed photonic platforms and thus increase the chip integration scale and density. As the monolithic scale of integration increases and acceptable yields are achieved, the penetration of monolithic technology on the hybrid

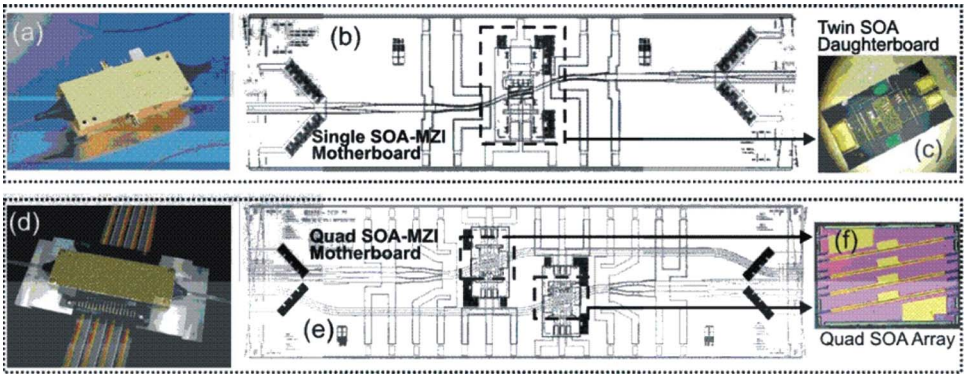

Fig. 1. (a) Packaged and pigtailed SOA-MZI optical gate, (b) corresponding motherboard design, (c) twin SOA silicon submounts, (d) packaged and pigtailed prototype device containing four SOA-MZI optical gates on a single photonic chip, (e) corresponding motherboard design, and (f) quad array of SOAs used for constructing each double SOA-MZI gate within the chip.

platform will be increased. This will eventually lead to an increase of integration density and more complex on-chip functionality while maintaining high yield and further cost reduction.

2.B. Ring Resonators

Tunable optical filters will be essential components in future reconfigurable optical networks. These should have ultranarrow bandwidth to be used in dense wavelength division multiplexing (DWDM) systems where the frequency spacing of the carriers is 50 GHz or less. On the other hand, the utilization of subcarrier multiplexed (SCM) data channels in DWDM optical networks has important potentials including packet addressing, performance monitoring using subcarriers, and network management and control. These systems require an efficient method to monitor, extract, and potentially erase subcarrier information. In this respect, optical filtering techniques have been used to simplify SCM receiver designs [18]. These filters must have high rejection ratios and free spectral ranges (FSRs) of tenths of gigahertz. Narrowband optical filters are also useful in photonic links that engage in high-speed optical rf signals. Another interesting approach is to have filter structures that can be monolithically integrated in a chip. Common filter technology available includes AWGs, thin-film dielectric interference filters (TTFs), conventional fiber Bragg gratings (FBGs), fiber Fabry–Perot (FP) filters, and MZIs. A complete review including most of these technologies can be seen in [19]. However, these devices have difficulty providing either notch or bandpass filters with ultranarrow bandwidths, reconfigurability, and tuning. Those requirements can be covered by optical filters based on ring resonators (RRs) [20].

These ring-based filters have been employed in numerous linear and nonlinear optical applications [21], including all-optical switches. Also compound ring resonators, which are constructed by a RR and a reflective section within it, are reported in [22]. Those filters are tuned by varying the phase delay of the waveguides, and the reflective section is implemented by a FP cavity or by a grating or a waveguide with a different refractive index. Tunable filters based on RR and a Michelson interferometer (MI) as the reflective element in the feedback path are reported in [23] with the MI made of a directional coupler and two identical Bragg gratings. The use of a Sagnac interferometer as the reflective element [24] allows a common-path architecture in the reflective section. Figure 2 shows the general architecture of a tunable filter based on a RR and a reflective section in the feedback path, working in its passive and active forms depending on the application. The filter response is calculated using the z-transform technique and simple design equations, when using a specific reflective section (a Sagnac loop), are reported. Tuning is achieved by changing the phase delay in the ring or Sagnac waveguides and additionally by changing the coupling coefficient of the Sagnac loop. In this case, up to a fourth of the FSR can be changed. Simple closed-form formulas describing the novel tuning process have been derived in its active and passive configurations, along with the requirements for having a certain operation as a bandpass or as a bandstop filter. In any of these configurations it is necessary to have a variable coupling coefficient, and its accuracy and tolerances are

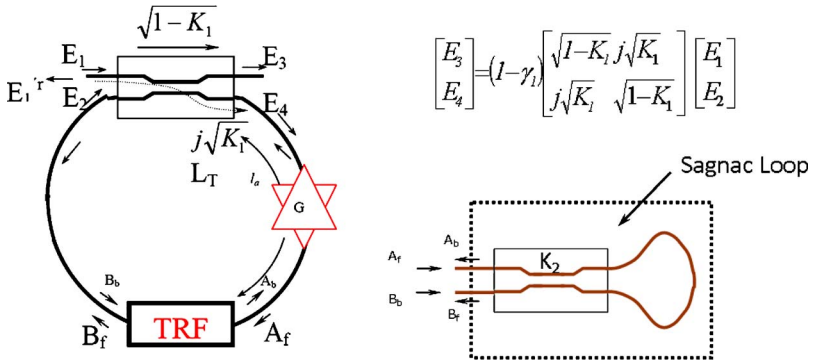

Fig. 2. General filter architecture. G is the optical gain that can be included in the loop for loss compensation. TRF is a general transmission-reflection function; a specific example is the Sagnac loop reported in the inset. L_T is the ring total length. K_1 and γ_1 are the coupling coefficient and excess loss of the coupler, respectively.

less than those of state-of-the-art technology. Also, as reported in [25], fabrication tolerance effects on a RR-based configuration can be controlled by using a variable loss or gain.

These filters can be implemented with optical fiber technology (microloops) with silicon or InP integrated optic technologies, since photonic circuits with equivalent components have already been developed. Some of them include a monolithically integrated Sagnac interferometer for an all-optical controlled-NOT gate, filters using active ring resonators, passive single- and double-ring resonators, and microcavities. The resonant frequencies of the proposed device can be shifted by changing the equivalent loop length by carrier injection or local heating as in any RR-based device. The transfer function can be tailored by changing the loop loss, and if III-V materials are used in the fabrication, this can be done by electroabsorption. The filter resonant frequencies can also be changed by tuning the coupling ratio, which up to now has been technologically possible by adjusting the taper–resonator gap fabricated by stretching a standard optical fiber with a micromechanical fiber variable ratio coupler, using microelectromechanical-systems- (MEMS-) actuated deformable waveguides [26] or using electrical control of waveguide resonator coupling in a Mach–Zehnder coupler configuration [27].

2.C. Wavelength Converters

Wavelength conversion has been identified as a key all-optical signal processing function related to advanced applications such as optical switching (through wavelength routing in passive devices such as AWGs) and contention resolution in dynamic wavelength assigned paths. Wavelength converters are based on the use of nonlinear elements that provide logic functions between two or more interfering input signals. The main nonlinear elements that have been extensively studied for wavelength conversion applications are SOAs, electroabsorption modulators (EAMs), highly nonlinear fibers (HNLFs), and periodically poled $LiNbO_3$ (PLLN) waveguides. Table 1 summarizes the main advantages and disadvantages of these elements.

Evidently, a preferred solution for wavelength conversion is not present because there is no element that shows advantages in all fields. As a general comment, HNLF has been successful in ultra-high-speed processing, but on the other hand the ability of SOAs to be hybridly integrated in advanced processing structures (such as MZIs) and their relatively small power consumption offers a more practical solution in possible future implementations. In terms of processing, wavelength converters have been implemented utilizing four main schemes.

Table 1. Nonlinear Elements and Their Advantages/Disadvantages for Signal Processing and Wavelength Conversion

	Integration	Footprint	Speed	Power Consumption	Other Comments
SOA	(√) High	(√) Small	(×) Limited (except in FWM effect or if advanced structures used, e.g., interferometers)	(√) Low (but increases if advanced SOA structures used)	(−) Introduces spontaneous noise in the system
EAM	(√) High	(√) Small	(−) Intermediate (limited but higher than SOAs)	(−) Low (but requires extra amplification due to absorption	(−) Low output power and added noise from amplification
HNLF	(×) Impossible	(×) Large (but can decrease with the use of fibers with a high nonlinear factor)	(√) High-speed processing	(√−×) Passive (but requires a high-input-power signal, therefore high amplification)	(×) Fiber introduces high losses

2.C.1. Cross-Gain Modulation (XGM)

In this scheme the initial data signal is combined with a continuous wave (CW) signal that denotes the new (converted) wavelength and both are inserted (Fig. 3) in a nonlinear active material (i.e., a SOA). The input powers must be carefully chosen so that the power of logic ones from the initial data saturates the nonlinear element. This has a direct effect on the gain (or absorption) that the CW signal faces, thereby modulating this CW at the desired output wavelength according to the power variations of the initial data [28,29]. The main advantages of XGM are the high conversion efficiency and the polarization insensitivity. However, the conversion speed strongly depends on the carrier dynamics, which are governed by the slow interband carrier recombination, thus limiting the operating speed. Thus bit rates faster than 40 Gbits/s cannot be realized easily, unless specially designed SOAs are used. For example, in [30], 100 Gbits/s wavelength conversion was achieved with a 2 mm long SOA and excessive performance penalty. Finally, the utilization of special offset filtering at the output of the SOA showed that it can significantly improve the conversion speed, allowing processing at 320 Gbits/s [31]. The aforementioned schemes refer to the copropagation mode of operation, although counterpropagation is beneficial in terms of filtering requirements, but limited in conversion speed. Prospects of achieving even higher bit rates lie in the use of quantum-dot-based devices. Pump-probe experiments reveal very fast gain dynamics in amplifiers made from this material (but it is yet to be proven in practice). In addition to speed limitations, the XGM converter has a number of drawbacks, such as data polarity inversion, relatively large output signal chirp (due to the large gain modulation), and wavelength-dependent extinction ratio performance.

2.C.2. Cross-Phase Modulation (XPM)

XPM is based on the phase shift induced on a signal when it propagates through a nonlinear device. The method is commonly applied on an interferometric approach able to translate the phase variations into amplitude variations. Such a scheme is shown in Fig. 4. In XPM converters, the optical input signal power controls the phase difference acquired by a pump along the two arms through the refractive index of the nonlinear element. At the output coupler, the phase difference is translated to power variation. The main principle of XPM has been implemented in various interferometric designs, namely, the delayed interference signal wavelength converter (DISC) [32], the MI [33], the MZI [34], the terahertz optical asymmetrical demultiplexer (TOAD) [35], the ultrafast nonlinear interferometer (UNI) [36], and the nonlinear loop mirror (NOLM) [37].

The interferometric converters have the advantage of very steep transfer functions enabling regeneration of the gated signals, but suffer from small dynamic range. Only low input-signal levels are needed to introduce a phase difference between the interferometer arms, so that a very efficient conversion is obtained almost independently of wavelength.

2.C.3. Four-Wave Mixing

The phenomenon of optical wave mixing is based on nonlinear interactions among the optical waves present in a nonlinear optical material. These interactions result in the generation of additional waves (products) as conjugative products of the initial ones. This mechanism is sensitive to both amplitude and phase information and in that sense is the only category of wavelength conversion method that offers strict transparency. There are two types of wave mixing demonstrated so far, even in field trials: four-wave-mixing (FWM) is based on the third-order optical nonlinearity and differ-

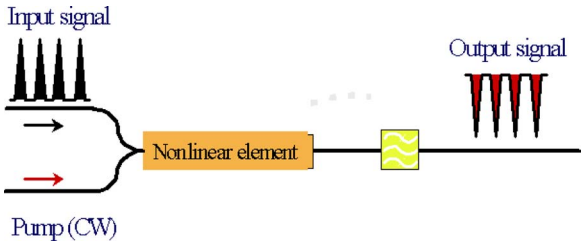

Fig. 3. Principle of operation for a XGM/XAM wavelength conversion scheme.

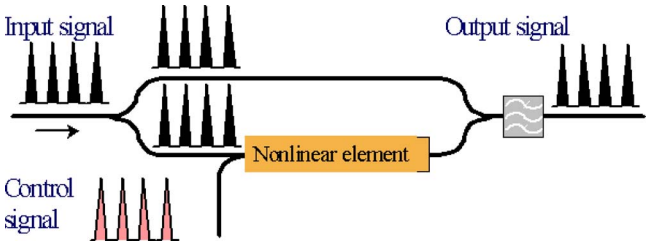

Fig. 4. Principle of operation for a XPM wavelength conversion scheme based on interferometric configuration.

ence frequency generation (DFG) is based on the second-order optical nonlinearity. One unique feature common among the converters of this category is that they allow simultaneous conversions of multiple input wavelengths to multiple output wavelengths. In what follows we further discuss FWM that has been thoroughly researched.

A schematic diagram of the FWM process is presented in Fig. 5. The beating of two waves at different frequencies modulates the polarization of the medium and a grating is generated. The interaction of the input waves with the gratings leads to new frequency components. The origin of FWM in SOAs [38,39] is related to intraband and interband carrier dynamics, whereas in fibers and passive devices, it is due to the induced polarization of the medium under an electric field. It should be noted that the presence of FWM is not restricted to SOAs and fibers; instead many nonlinear materials exhibit FWM effects. FWM in SOAs is attractive, despite the added amplified spontaneous emission (ASE) that degrades the optical signal-to-noise ratio (OSNR). The latter drawback is counterbalanced by the compactness of SOA-based devices, which enables integration. A major advantage of FWM is that it supports the simultaneous conversion of multiple wavelengths. The disadvantage of FWM is its low conversion efficiency, which results in low-power FWM products. The main parameter that affects both the efficiency and OSNR is the unsaturated gain, which can be enhanced by utilizing either longer SOAs with a smaller active layer or different structures such as multiple-quantum-well devices.

These problems can be solved with the use of dual-pump FWM (d-p FWM) configurations [40], which are able to provide ultrawide conversion bandwidth with almost uniform performance over the whole range, without distinguishing between upconversion and downconversion. Moreover, d-p FWM configurations have been proposed as polarization-insensitive solutions using polarized pumps or polarization diversity techniques. However, due to the nature of the nonlinearities, the main advantageous characteristic of FWM, compared with the other conversion schemes, is its ability to support ultrahigh bit rates, beyond 160 Gbits/s, without the need for complicated configurations or specially designed materials.

2.C.4. Wavelength Conversion in Quantum-Dot SOAs

A newly advanced technology that promises optical signal processing operations at high bit rates as well as multiwavelength processing capabilities is based on the use of quantum-dot SOAs (QD-SOAs). These capabilities originate from the physical properties of quantum dots that offer significant advantages over the conventional bulk and even quantum-well-based SOA devices. The response time of the saturated gain is of the order of 100 fs to 1 ps, which leads to negligible patterning effect. The spatial isolation of dots leads to spectrally localized effects and thus to cross-talk suppression

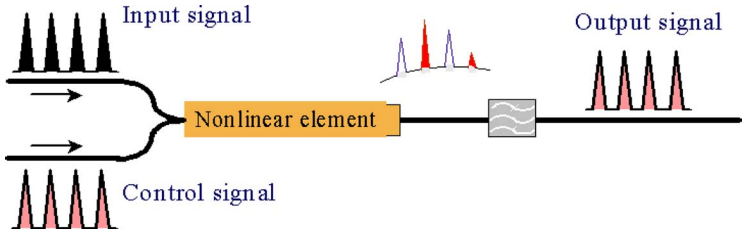

Fig. 5. Principle of operation for a FWM wavelength conversion scheme through a nonlinear element.

between WDM channels under gain saturation conditions. On the other hand, wavelength channels that have a similar energy level present a strong interaction leading to an effective XGM of the saturated gain, which can be utilized for switching operation when channels are within the homogeneous broadening of the single-dot gain. However, quantum-dot SOAs are still an immature technology and only limited experimental demonstrations have been performed, which have although revealed advantageous performance characteristics, such as ultrafast gain recovery times or uniform FWM wavelength conversion independent of the pump-probe relative spectral position [41] (i.e., upconversion or downconversion).

3. State of the Art in Wavelength Conversion

Recent advances in wavelength conversion relate to the demonstration of nonlinear FWM, multiwavelength conversion/regeneration, as well as QD-SOA-based conversion. The FWM technique is an attractive wavelength conversion solution due to its intrinsically ultra-high-speed properties that allow rapid conversion of data streams transmitted at ultrahigh bit rates. Specifically, the use of SOAs may offer a compact integrated and particularly economical solution in the development of an array of wavelength converters within a single chip. Techniques that have been used to demonstrate wavelength conversion include dual-pump FWM, pump filtering in FWM, and XPM in a SOA. In what follows we present the main achievements of these efforts.

3.A. Nonlinear FWM Effect in a Semiconductor Optical Amplifier

In this subsection, wavelength conversion at 40 Gbits/s with return-to-zero (RZ) data signals is demonstrated using a single-pump scheme based on FWM in a SOA, while some specific considerations are pointed out. Using this technique, it is important to carefully adjust input powers and wavelengths to achieve optimum FWM performance. Because previous measurements have been carried out using non-return-to-zero (NRZ) data signals, here the [on–off-keying (OOK)] RZ data format has been chosen because it appears to be more appropriate for high-speed data transmission. Also, in doing so, possible pattern effects (XGM-based modulated CW pump at the output of the SOA), which may result in a spectral overlap with the wavelength converted data, have been investigated. The study has been realized by means of experiments using the setup described as follows.

In Fig. 6 the experimental setup used for this investigation is shown. The 40 Gbits/s RZ data transmitter is composed of a 10 GHz repetition-rate pulsed mode-locked fiber laser (MLFL), whose pulses were optically multiplexed using a fiber delay line multiplexer (OMUX) to 40 GHz before they where modulated with an external

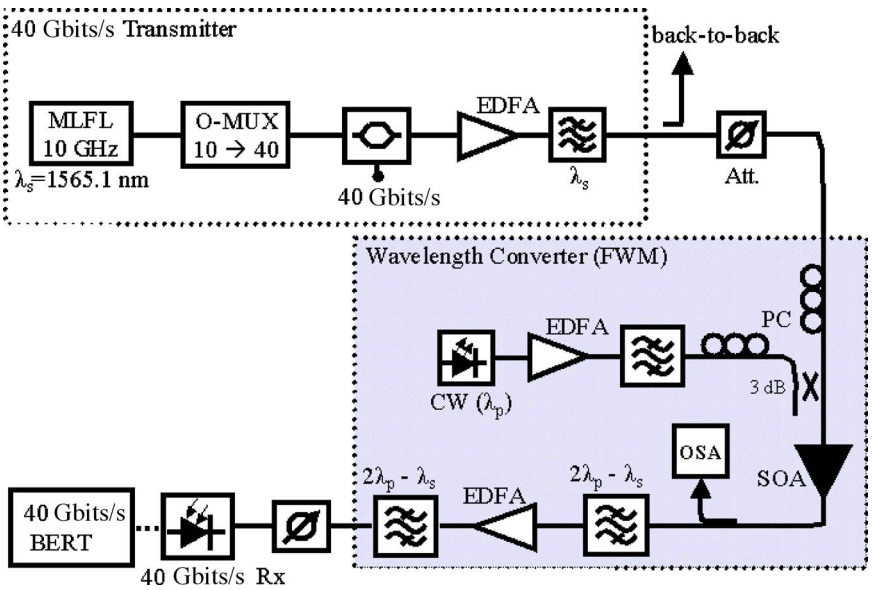

Fig. 6. Experimental setup for wavelength conversion using FWM in a SOA.

Mach–Zehnder modulator and amplified by an erbium-doped fiber amplifier (EDFA). A filter was placed to eliminate ASE noise from the data signal. To vary the input power of the data signals, an optical attenuator was placed before the wavelength converter. The wavelength converter was comprised of a CW pump laser at λ_p, a SOA as a nonlinear medium, two EDFAs, several optical filters to reduce the accumulative ASE noise, and two polarization controllers because FWM is a polarization-dependent effect.

The data and pump signals were merged using a 3 dB coupler, whose output was directly connected to the SOA, where the FWM effect takes place and the FWM product is generated at a wavelength of $2\lambda_p - \lambda_s$. This is also the wavelength where the two optical filters at the output of the SOA and EDFA, respectively, were centered. Bit-error-rate (BER) measurements were carried out by varying the data input power into the wavelength converter for different pump powers and also for different pump wavelengths (1560.0, 1563.2, 1563.7, and 1564.2 nm). The FWM conversion efficiency and optical spectra for different system parameters were also measured at the output of the SOA using an optical spectrum analyzer (OSA). As already mentioned above, the influence of different system parameters (input signal powers and wavelength separation between the data and the pump) on the system performance has been studied by the evaluation of the system penalty (in comparison with the back-to-back measurement) using the BER criteria. To evaluate the quality of the above-described wavelength converter, the input signal power has been varied for three different pump powers at a fixed wavelength allocation ($\lambda_p = 1563.7$ nm) and the penalty has been calculated at a BER of 10^{-9}. Figure 7 shows the obtained penalty curves varying the input data power for different pump powers and a pump wavelength of 1563.7 nm. It is shown that the minimum power penalty is nearly the same for all the pump powers, but the signal power range is different for each pump power. Generally, high pump powers produce a shift of the optimum signal power toward higher values, whereas the opposite occurs for low pump powers. This result confirms the previously inferred design rules for 10 Gbits/s extending its application range for 40 Gbits/s signals. That is, optical signal power must be approximately 10 dB lower than the pump power to achieve optimum performance in a one-pump-based FWM wavelength converter.

In a next step, the input data power was varied for different pump wavelengths at a fixed pump power of 10 dBm, which has been shown to be the most appropriate power to achieve best performance in a higher range of input data powers. The

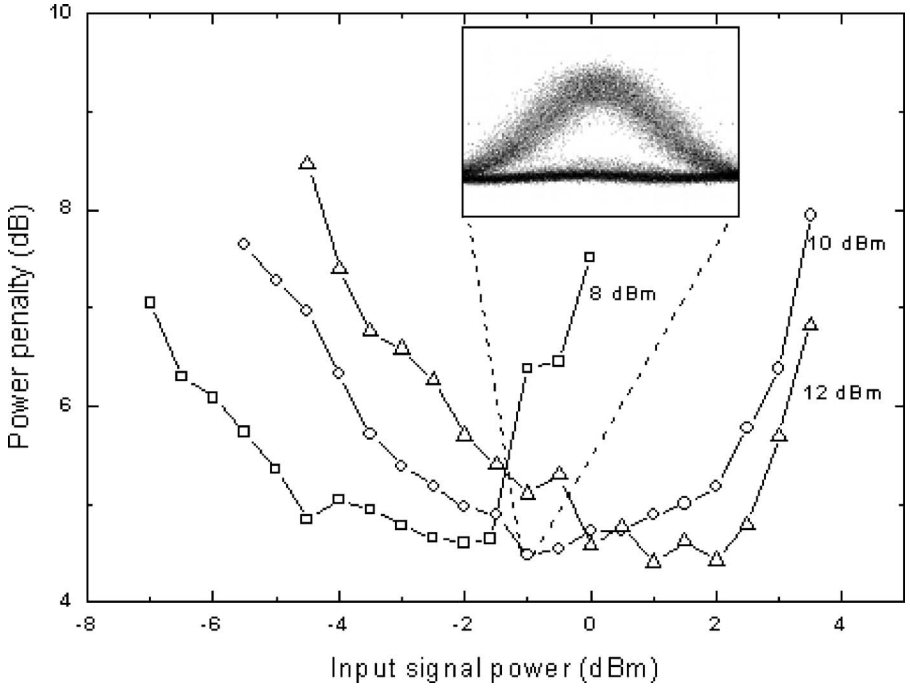

Fig. 7. Power penalty as a function of input signal power for different pump powers and a pump wavelength of 1563.7 nm.

obtained results, also expressed in penalty curves, are shown in Fig. 8. It is clear that there is an optimum range of input signal powers for which the power penalty varies less than 1 dB. Here again, the design rules previously obtained are extended to 40 Gbits/s operation. That is, pump wavelengths closer to the signal wavelength provide lower penalty due to a higher FWM conversion efficiency. However, there is a limit for which some distortion effects arise, in the case of high bit rates as in the experiment. In that case, the modulation peaks in the pump wavelength caused by XPM distort the converted data signal when high input signal powers are used. Therefore, to achieve optimum performance, the optimum pump wavelength was found to be approximately 1.3 nm lower (about 4 times the bit rate of the input signal) than the signal wavelength.

3.B. Tunable 160 Gbits/s Wavelength Multiwavelength Converter Based on Supercontinuum Generation in a Highly Nonlinear Fiber

An important feature of the network nodes is the capability to multicast a high-bit-rate signal by creating multiple replicas at different wavelengths. Nevertheless only a few attempts at 160 Gbits/s multiwavelength conversion have been demonstrated. In [42], a CW laser is necessary for each output wavelength. Spectral broadening induced by supercontinuum (SC) generation followed by multibandpass optical filtering allows a high-bit-rate signal to be converted to several wavelengths without additional CW lasers, thus potentially leading to a lowering of the overall node cost. By this technique we have demonstrated upconversion and downconversion of a 160 Gbits/s signal to two new wavelengths [43]. The wavelength conversion is obtained exploiting SC generation in a commercial HNLF. The experimental setup is shown in Fig. 9.

The pulse source is a polarization-maintaining fiber ring mode-locked laser (ML-FRL) at 10 GHz. The pulses are modulated with a Mach–Zehnder modulator (MZM) driven by a 10 Gbits/s data sequence. The pulses are then compressed down by a soliton compressor to increase the pulse peak power, enhancing the supercontinuum generation. Afterwards the 10 Gbits/s signal is multiplexed to 160 Gbits/s. The 160 Gbits/s signal is amplified and injected into the HNLF to achieve spectral broadening by supercontinuum generation. The HNLF has a flat dispersion profile at 1550 nm. The 160 Gbits/s wavelength converted signal is obtained by slicing the supercontinuum spectrum with a tunable filter bandwidth. To evaluate the performance of the proposed wavelength multiconverter, the converted signal is demultiplexed to 10 Gbits/s by exploiting FWM in a second HNLF. The control pulses at

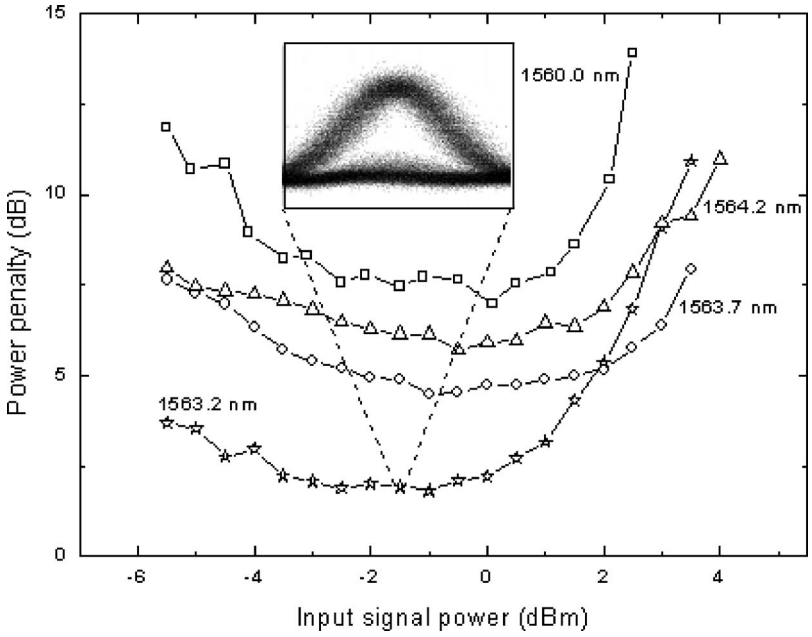

Fig. 8. Power penalty as a function of the input signal power for different pump wavelengths and a pump power of 10 dBm.

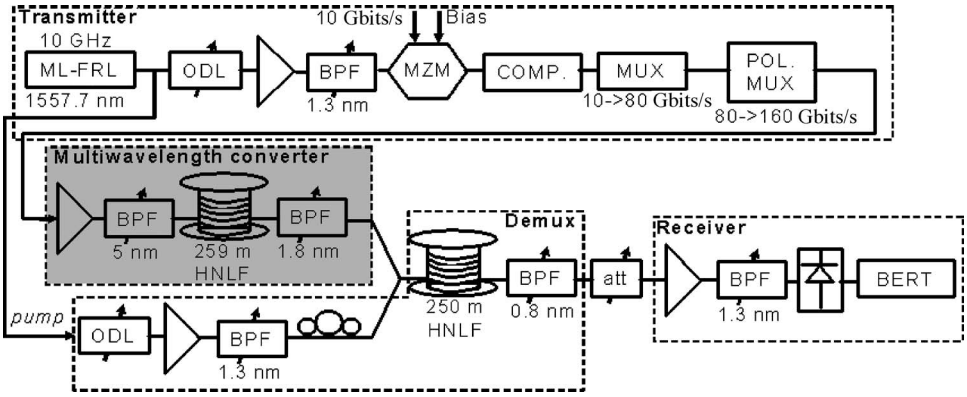

Fig. 9. Experimental setup of the tunable multiwavelength converter.

1557.7 nm are split from the 10 GHz pulse source. The BER is measured on the channels of each wavelength converted 160 Gbits/s signal.

The wavelength of the converted channels can be tuned acting on the input power: a detuning up to 8.5 nm is obtained at the input of the first HNLF. With an input peak power, two high-quality replicas (upconverted and downconverted) of the 160 Gbits/s signal are generated with an optimum detuning, with respect to the input signal, of 4.2 and 5 nm, respectively. Figure 10 shows the eye diagrams of the two polarization multiplexed 80 Gbits/s signals of the upconverted [Fig. 10(b)] and downconverted [Fig. 10(a)] 160 Gbits/s signals. BER measurements are performed under these conditions. Figure 10(c) shows the BER of a demultiplexed random tributary channel for upconverted and downconverted replicas compared with the back-to-back signal. Bit-error-rate measurements reveal error-free performance for each of the tributary channels of the 160 Gbits/s converted replicas. The different slopes of the BER curves of the upconverted signal are due to the nonuniform spectral broadening of the supercontinuum, which leads to different optical signal-to-noise ratios.

3.C. Wavelength Conversion Using QD-SOAs

QD-SOAs have been reported as a candidate technology to provide multiwavelength operation at high bit rates [41,44]. When channels are within the homogeneous broadening of a single-dot gain, then the fast XGM effect of QD-SOAs can be exploited for parallel (multiwavelength) switching/regeneration operation. Here we report the results of an all-optical multiwavelength (2R) regenerator using two cascaded QD-SOAs at 40 Gbits/s [45]. The regenerator configuration is illustrated in Fig. 11(a). Two QD-SOAs in cascade are used to enable wavelength conversion between the modulating pump and CW probe signals, respectively. The two input channels carry the data at wavelengths λ_1 and λ_2, which serve as pump signals. The latter modulate

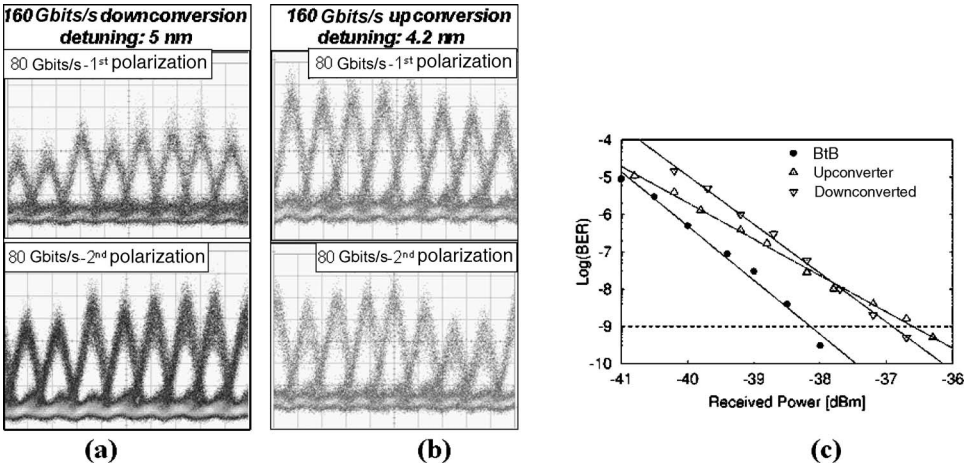

Fig. 10. Eye diagrams of the 160 Gbits/s (b) upconverted and (a) downconverted signals for the two interleaved polarizations (top and bottom). (c) Corresponding BER curves for a random upconverted and downconverted tributary channel.

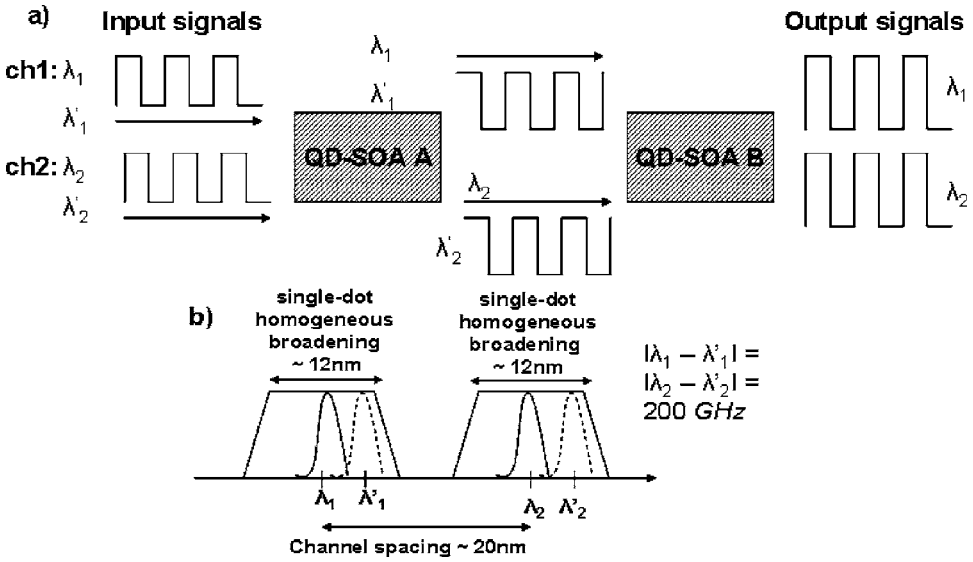

Fig. 11. (a) Subsystem description. (b) Two channels within the inhomogeneously broadened gain spectrum of the QD-SOA.

the carrier density with subsequent modulation of the refractive index, the phase, and the gain of the QD-SOA. This gain modulation effect is isolated within a fairly narrow spectral region around the wavelength of each pump. Therefore, it is experienced mostly by the corresponding probe signals (λ_1' and λ_2'), which are detuned by 200 GHz with respect to the pump signals. As illustrated in Fig. 11(b), the two channels are spaced 20 nm apart within the inhomogeneously broadened gain of 90 nm. The bit stream for each input channel consists of 8 ps first-order Gaussian pulses, with an extinction ratio of 13 dB at 40 Gbits/s.

At the output of QD-SOA A the data of both channels are copied to the (CW) probe signals and inverted. A passband filter is used to remove the amplified pump signals originally located at λ_1 and λ_2. The output probe signals of QD-SOA A at wavelengths λ_1' and λ_2', which carry the input information inverted, serve as pump signals to the input of QD-SOA B. Two new (CW) signals at λ_1 and λ_2 serve as probe signals input to QD-SOA B. As a result, information initially carried by the two input channels has been reinverted and regenerated at the output of the subsystem. To represent the performance of the QD-SOA devices in this regenerative configuration setup, we employed the model proposed in [46]. The referenced model has been developed accordingly to serve as a tool for simulation studies taking into consideration multiwavelength operation.

To demonstrate efficient regenerative performance, we need not only to ensure extinction ratio preservation but also to achieve suppression of the amplitude fluctuation. The latter has been quantified by defining as a figure of merit the Q-factor ratio $[\Delta Q = 10 \log(Q_{\text{out}}/Q_{\text{in}})]$. P_{probe1} represents the power of the probe signals at the input of QD-SOA A, whereas P_{probe2} represents the corresponding power level of the probe signals at the input of QD-SOA B. The two channels (ch1 and ch2) at the input of the subsystem are spaced at 20 nm and have an average power of +22 dBm. The length of both devices QD-SOA A and QD-SOA B is considered to be 10 mm. Furthermore, the input pulse streams suffer from amplitude distortion at the level of ones, bearing a low Q factor (Q factor$_{\text{ch1}}$=5.7, ext_ratio$_{\text{ch1}}$=13 dB, Q factor$_{\text{ch2}}$=5, ext_ratio$_{\text{ch2}}$=13 dB). Further simulations have been performed to optimize the operation point of the QD-SOAs when two input channels are present. Figures 12(a) and 12(b) illustrate the extinction ratio and Q-factor improvement as a function of P_{probe1} and P_{probe2} for channel 1. The numbers in the contour graph represent the corresponding degradation or Q-factor improvement.

It is clear that the extinction ratio is severely degraded as P_{probe2} increases. This is something expected for the XGM effect. On the other hand, high power levels of P_{probe1} are required in order to achieve sufficient pump powers at the input of QD-SOA B. This results in extinction ratio enhancement at the second stage of the subsystem. Similar performance in terms of extinction ratio is observed for channel 2

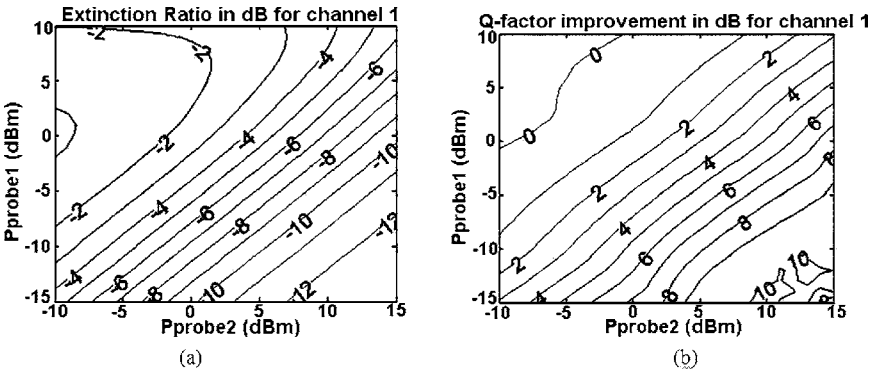

Fig. 12. (a) Extinction ratio and (b) Q-factor improvement as a function of Pprobe1 and Pprobe2 for channel 1.

as well. This has been attributed to the fact that channel 1 and channel 2 are located symmetrically around the central wavelength of the inhomogeneously broadened gain profile. Significant Q-factor improvement has been observed for larger values of P_{probe2} in contrast to the extinction ratio. This is associated with the fact that both QD-SOAs operate beyond the saturation power where the transfer function slope is very steep. It is obvious that all-optical regeneration has been achieved for both channels. Amplitude fluctuation at the level of ones has also been suppressed resulting in Q-factor improvement of 2.7 dB for channel 1 and 3 dB for channel 2. The extinction ratio may be improved with the use of a saturable absorber.

4. State of the Art in All-Optical Subsystem Design

4.A. All-Optical Packet Processing Subsystems

The evolution from single-gate experiments to more complex all-optical subsystems was made possible due to the development of compact SOA-MZI-based optical gates, exploiting a unified integration platform based on hybrid technology [13,17]. This photonic integration platform is a pragmatic combination of the best available optical technologies for active and passive optical devices toward the implementation of a true all-optical packet router. Figure 13 shows a block diagram of the basic functionalities required to realize an all-optical packet switched node, including time-slot reordering, wavelength conversion, bit-level synchronization, regeneration, label processing, and packet switching.

The clock recovery subsystem performs bit-level synchronization, whereas the CDR is performed for 3R regeneration of the incoming traffic. On the other hand, the label/payload separation subsystem is used to forward the extracted label to the label processing unit and the separated payload to the switching matrix. The time-slot interchanger circuit is used to buffer packets and resolve contention. Optical buffering has been investigated in a plethora of architectures that incorporate optical switches

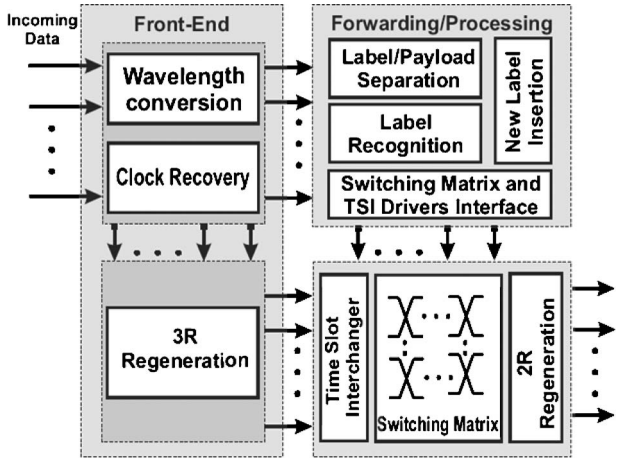

Fig. 13. Top-level design of an all-optical packet switching node.

and feedback and feed-forward fiber delay lines [47], and recent advances in optical integration have enabled the demonstration of an integrated optical buffer. In this subsection, the implementation of an all-optical CDR and a header extraction circuit for 40 Gbits/s packet-mode traffic are demonstrated [48], while the implementation of the time-slot interchanger circuit is presented in the next subsection. The first two circuits have been built with three generic, hybrid-integrated, MZI switches and a fiber FP filter, whereas the latter has been implemented using a quadruple array of SOA-MZI switches of hybrid integration on a single chip [49].

Figures 14(a) and 14(b) respectively show the corresponding CDR and label/payload separation experimental setups. Both setups consist of a 40 Gbits/s optical packet generator, a wavelength converter, which is used to locally control the wavelength and the carrier phase of the incoming signal, a clock recovery circuit, and a third MZI gate used to act as the decision gate at the CDR circuit or to perform the final separation of label and payload data at the label/payload circuit. In addition, a 40:10 demultiplexer was also employed in both circuits in order to obtain BER measurements at 10 Gbits/s. In both circuits, the same 40 Gbits/s optical packet generator was used to obtain data packets at 40 Gbits/s. For the case of the CDR circuit, additional electrical circuitry was built to introduce rms phase jitter at the generated short pulses. The 40 Gbits/s test signal was then split and fed to the wavelength converter (WC) section as well as to the third MZI gate [see Figs. 14(a) and 14(b)]. After wavelength conversion, the signal is amplified and injected into the clock recovery (CR) circuit to achieve all-optical timing extraction. The CR employed a low-Q fiber Fabry–Perot (FFP) filter with a FSR equal to the line rate (40 GHz), as well as a SOA-MZI powered by a CW signal, operating as a holding beam. A 2 bit preamble is used in the beginning of the packet for both cases to assist the clock extraction process.

In the case of the CDR circuit, the recovered clock is then used as the input signal to the third MZI, where the incoming data served as the two differential controls. Retiming and reshaping are achieved through optical sampling of the degraded data onto the retimed optical recovered clock pulses [48]. Similarly, at the label/payload circuit [see Fig. 14(b)], label and payload separation is obtained in MZI3, which is configured to perform an AND operation between the input data signal and the properly delayed recovered packet clock. Successful label/payload separation is obtained by delaying the packet clock with respect to its respective data packet for an interval equal to the original packet label. In this way, the payload of the original packet appears at the switched port of the MZI, whereas the label exits the gate via its unswitched port. The extinction ratio at the output of MZI3 was improved with the use of a counterpropagating CW signal. To verify performance of both circuits, BER measurements were performed after demultiplexing the 40 Gbits/s output signals into 10 Gbits/s data streams using an EAM as a demultiplexer.

The CDR performance was tested with short data packets of different durations and the results obtained are summarized in Fig. 15. In particular, the oscilloscope

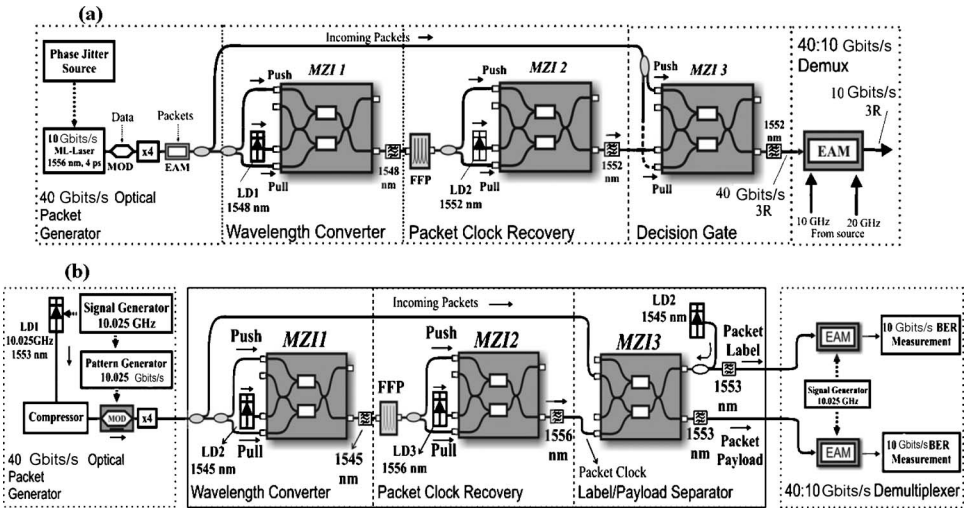

Fig. 14. Implementation of (a) clock and data recovery and (b) label/payload circuit using three generic, hybrid-integrated, MZI switches and a fiber Fabry–Perot filter.

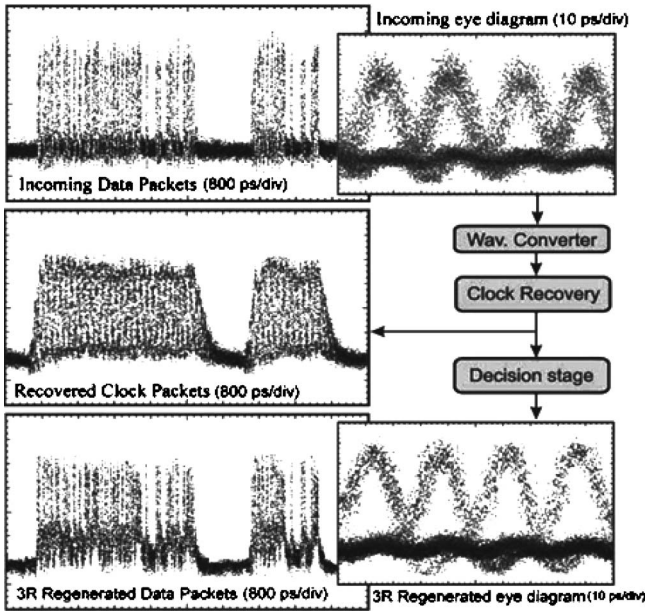

Fig. 15. Results obtained through the 3R regenerator subsystem.

traces of the incoming degraded 40 Gbits/s packets, the recovered clock packets, and the regenerated data are illustrated in parallel to the respective eye diagrams. The recovered clock packets are obtained at the output of the clock recovery stage ensuring clock persistence for duration equal to the corresponding data packet length increased by the rise and fall times of the clock, respectively. The eye opening of the regenerated signal demonstrates phase and amplitude jitter reduction when compared with the eyes of the incoming data. The jitter reduction originates from the FFP filter transfer function, which is centered on the carrier, suppressing the data harmonics and thus reducing the phase jitter of the recovered clock.

Figure 16 illustrates the label/payload separation process through trace diagrams obtained at each stage of the circuit in parallel to the respective eye diagrams. Figure 16(a) shows two incoming data packets of different lengths, and Fig. 16(b) shows the respective wavelength converted packet stream. Figure 16(c) shows the recovered clock packets as they have been delayed by a time interval equal to the label length. Figures 16(d) and 16(e) show the separated labels and payloads, obtained at the output of MZI3.

4.B. All-Optical Time-Slot-Interchanger Architecture

Optical buffering is a key issue that still has to be addressed for the realization of high-speed packet switched optical networks (OPS), since it enables performing crucial functionalities such as contention resolution and traffic shaping. Optical buffering has been investigated in a plethora of architectures that incorporate optical switches together with feedback or feed-forward fiber delay lines. Such implementations that are based on programmable delay lines maintain the advantages of lower energy per written/read bit and smaller power dissipation, as compared with electronic buffers [50] and have been extensively used to form feed-forward or recirculating architectures, employing in addition wavelength conversion to enhance buffering capabilities [51,52]. Recent advances in optical integration have enabled the demonstration of an integrated optical buffer [53], while other attempts include either other technologies, as, for example, slow-light optical delay lines [54]; polarization bistable VCSELs [55]; or other switching architectures such as the Vortex switch [56].

In this subsection, we present results of an all-optical time-slot-interchanger circuit using for the first time to our knowledge a quadruple array of SOA-MZI switches of hybrid integrated on a single chip [57]. Their high-speed processing capability and integrability into compact arrays enable the implementation of optical buffers that employ cascades of switching elements.

The proposed system architecture is presented in [58]. It comprises cascaded programmable delay stages and each stage consists of a wavelength converter that pro-

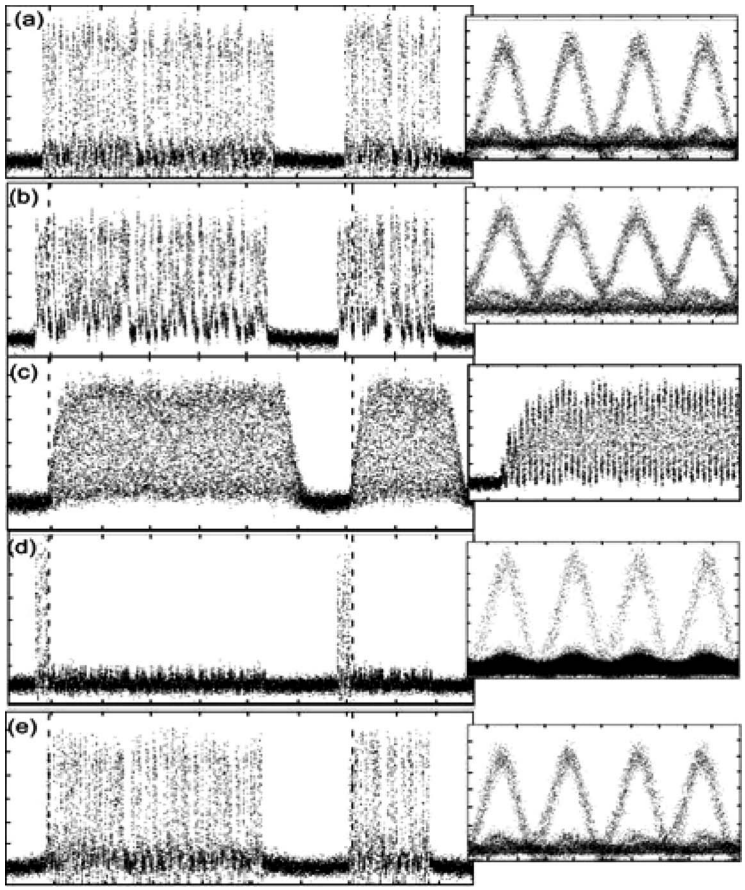

Fig. 16. Trace and eye diagrams of (a) the incoming data packets, (b) the wavelength converted packets, (c) the packet clock recovery and its rise time, (d) the extracted label, and (e) the extracted payload. The time scale is 1 ns/div for the traces, 200 ps/div for the clock recovery rise time trace, and 10 ps/div for the eye diagrams.

vides w separate wavelengths at its output and a bank of w parallel delay lines, one per wavelength. The wavelength converter assigns the incoming packets with wavelengths according to the delays they will experience, while each packet accesses the assigned delay by means of a wavelength demultiplexer. The delays that are introduced at each time-slot interchanger (TSI) stage are a design parameter of the proposed architecture [58]. The experimental demonstration of the proposed architecture has been performed for $w=3$ and three stages as shown in Fig. 17. It consists of a 10 Gbits/s NRZ data packet generator, a three-wavelength control scheduler, the 10 Gbits/s TSI circuit, the routing control unit, and a fiber-coupled saturable absorber (SA) mounted on a circulator. The wavelength control scheduler involves three CW signals, which are multiplexed and modulated into packet envelopes that coincide in the time domain. These envelopes are introduced into a delay configuration comprising demux/muxes and fiber segments of fixed length. A sequence of three consecutive packet envelopes of the same length and different wavelength is thus obtained at the mux output. This signal then enters a polarization beam splitter (PBS) so that a specific polarization component from the three wavelengths can be picked out and then split into three parts, which form the input signals of the three stages of our circuit. The time slots that the packet envelopes occupy and their corresponding wavelengths at the output of the routing control unit have been assigned using appropriate time-slot and wavelength assignment algorithms presented in [58].

Each TSI stage deploys a SOA-MZI switch and a demux/mux-based programmable delay bank. The MZI operates as a wavelength converter, based on the cross-phase modulation effect caused by the control signal, assigning each packet that appears at its control port with one of the three input wavelengths. The delay bank delays each incoming packet according to the wavelength it has been assigned. As a result, incoming packets are interchanged at the stage output based upon the wavelength assign-

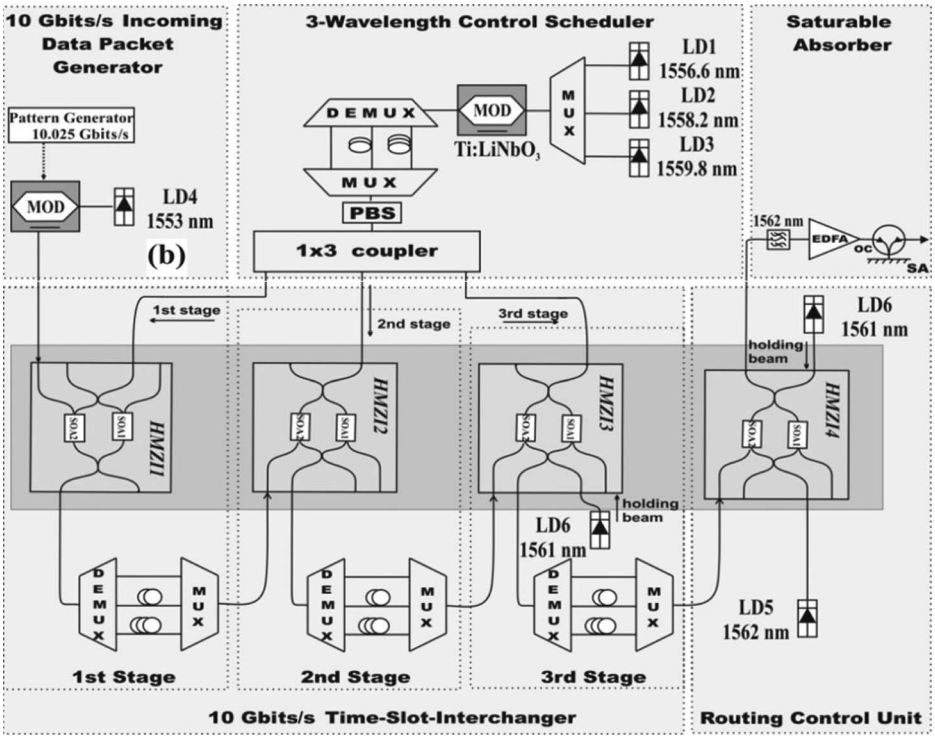

Fig. 17. (a) Proposed buffer architecture and (b) experimental setup.

ment procedure. The fiber segments of each delay bank correspond to zero, one, and two time slots for the first stage; zero, two, and four time slots for the second stage; and zero, one, and two time slots for the third stage. The wavelength-converted packets at each stage output are fed to the control port of the next-stage MZI in a counter-propagating control/input signal fashion except for the first stage. The fourth MZI acts as a routing control unit that translates the three-wavelength output of the TSI to a single wavelength for appropriate routing in a wavelength-routed node. A holding beam enters MZI3 and MZI4 to reduce ASE and increase the extinction ratio of the output signals, while the saturable absorber is used to enhance signal quality through noise reduction and pulse narrowing.

Figure 18 demonstrates the BER measurements obtained at the output of each stage. Error-free operation was achieved with power penalties of 0.2, 0.78 , 1.43, and 1.8 dB after the first, second, and third TSI stages and the routing control unit, with respect to the input signal. The gradually increasing power penalty is primarily a result of eye closure due to pulse broadening from the gain saturation and recovery dynamics of the SOAs.

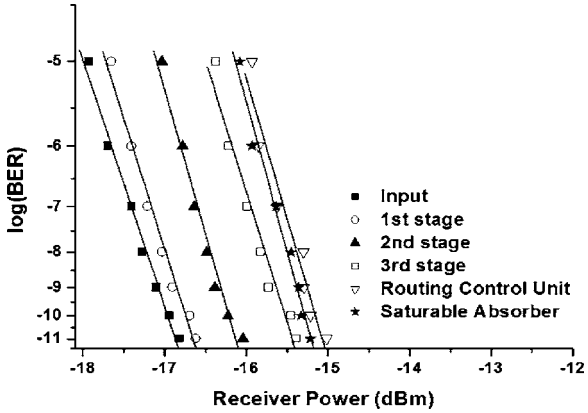

Fig. 18. BER measurements at the output of each stage of the all-optical time-slot interchanger circuit.

4.C. Optical Gates and Flip-Flops

In future photonic networks including optical technologies such as optical packet switching, all-optical bistable devices will be key elements for packet buffering, self-routing, and bit-length conversion [59]. A few devices and architectures for all-optical flip-flops have been demonstrated so far, mainly based on the bistable operation of laser diodes and semiconductor optical amplifiers. In particular, bistable laser diodes, such as vertical-cavity surface-emitting lasers [60] and coupled laser diodes [61], have been investigated for the realization of all-optical flip-flops.

A novel approach for optical flip-flops, which exploits absorption and fluorescence in erbium–ytterbium-doped fiber [62], has been proposed. The high stable level of an optical flip-flop can be associated with the transparency state of the erbium–ytterbium-doped fiber, whereas the low stable level refers to the absorption state of the same fiber without excitation. The bistable flip-flop output is obtained by injecting a low power reading signal in the fiber span: if such a signal reaches the output port, the stored level is high; on the contrary, when the signal is completely absorbed, the stored level is low. The set signal is a strong energy optical pulse at a wavelength close to the maximum erbium absorption cross section. The reset pulse is at a wavelength where stimulated emission dominates. The proposed architecture allows a long memorization time of the high stable output level (over a microsecond range) and the possibility of obtaining transition times as short as the set and reset pulse widths. Moreover, erbium–ytterbium waveguides can be integrated, reducing the footprint and the cost of the optical flip-flop. Nowadays Er-doped waveguide amplifiers are on the market; i.e., the technology for the integration of Er-doped waveguides is mature. With integrated technology, an Er-doped waveguide of a few centimeters (2–3 cm) can provide the same gain as a 1 m long Er–Yb-doped fiber. The experimental setup is shown in Fig. 19.

A continuous wave at λ_S is used to obtain the flip-flop set signal. The set pulsed signal is obtained using a programmable electric wave generator and a Mach–Zehnder modulator (MZM1). In the same way, the reset pulsed signal is generated, through a tunable laser, at λ_R, modulated by MZM2. Both signals are then coupled into 1.5 m of erbium–ytterbium-doped fiber. Figure 20(a) shows the optical spectrum of coupled set and reset signals at the doped fiber input. The reading signal is generated by a CW source, and it is launched through the doped fiber in the counterpropagating direction with respect to the set and reset signals. In this experiment the reading signal wavelength is λ_P, even if in principle, it can be tuned over the entire erbium fiber bandwidth. We realized a counterpropagating configuration using a circulator, and thus in this way set and reset input signals propagate from port 1 to port 2 of the circulator reaching the input of doped fiber, while the counterpropagating reading signal, after

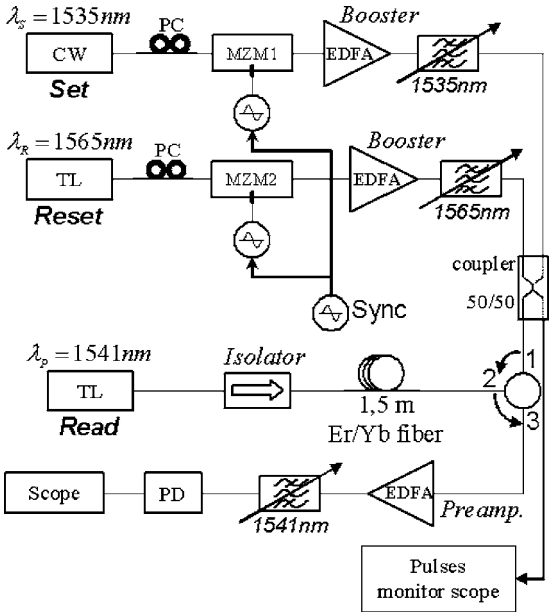

Fig. 19. Experimental setup of the optical flip-flop.

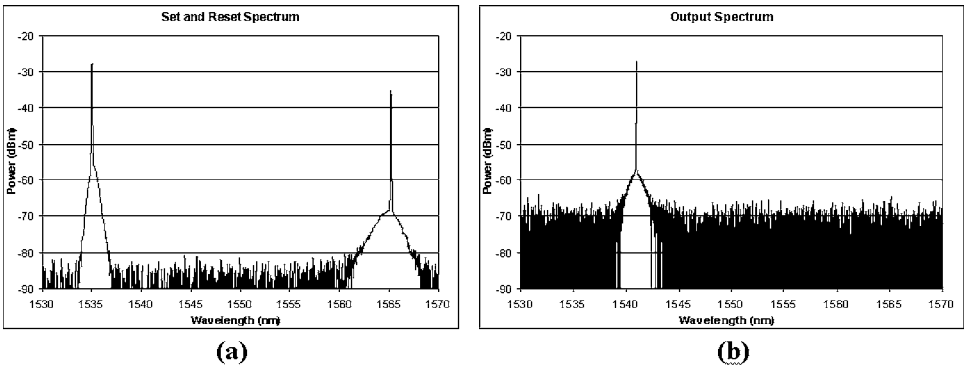

Fig. 20. Optical spectra for (a) set and reset pulsed signals and (b) output reading signal.

the output of the fiber, propagates from port 2 to port 3. The spectrum of the output reading signal is shown in Fig. 20(b). Finally the reading signal is amplified by a low-noise preamplifier and then photodetected and visualized through an oscilloscope. Set and reset pulses are shown in Fig. 21(a), whereas the output reading signal is shown in Fig. 21(b). The repetition frequency of set and reset pulse trains is ~900 kHz, both having a pulse width of approximately 10 ns. The set pulse energy is 18.5 nJ, whereas the reset pulse energy is 19.8 nJ. The high output power level is maintained for 422 ns, but it can be considered constant for dozens of microseconds. Rising and falling times are of approximately 10 ns, but they can be shortened to less than 1 ns by increasing the set and reset signal power and decreasing their pulse width.

5. State of the Art in Optical Ring Resonators

Other key optical components of photonic subsystems are those that perform the function of splitting (demultiplexing) very narrow channels (wavelengths). Demultiplexing requires optical spectral filters and is a challenging problem when real system constraints are applied. Common techniques for making demultiplexers are MZI-based devices, which include waveguide grating routers (WGRs), thin-film filters (TFFs), Fabry–Perot filters, RR filters, and FBGs. The simplest design in terms of raw material and technologies is a fused-fiber MZI. By hybridizing some technologies such as MZIs, AWGs, dielectric TFFs, and FBGs, DWDM systems can be upgraded into much narrower channel spacing for very large capacity applications. This is also the intention of the device proposed here—hybridizing MZI interferometers and RR [25] to achieve ultranarrow spacing, higher channel isolation, and design flexibility.

Active devices are designed to avoid losses and for design flexibility purposes. However, the gain must be controlled so that the filter does not become unstable. They have a narrow full width at half-maximum (FWHM) and the design flexibility of amplified ring resonators while the FSR limitation is overcome by using cascaded MZIs. The MZIs also allow demultiplexing and deinterleaving. These devices have much better cross-talk immunity performance than sinusoidal Mach–Zehnder interleavers and demultiplexers, but not as good flattop and broad passband as asymmetric Mach–Zehnder interleavers and demultiplexers. An example of a 1×4 demultiplexer is reported in Fig. 22. There are two MZI stages and one RR, with $\Delta L_1=2\Delta L_2$ and $L=2\Delta L_1$, where L is the RR loop length. The FSR of the $1\times N$ demultiplexer, denoted as FSRT and the FSR of the RR are related by

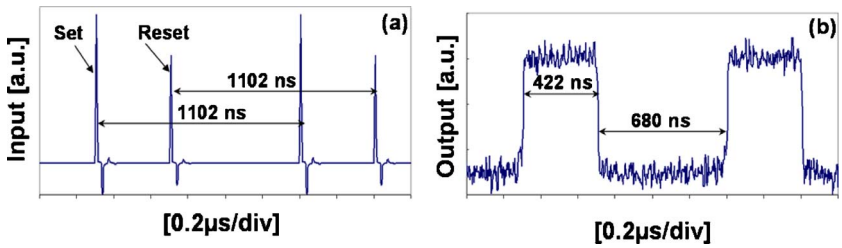

Fig. 21. Periodic flip-flop operation signals: (a) set and reset input pulses, (b) output reading signal.

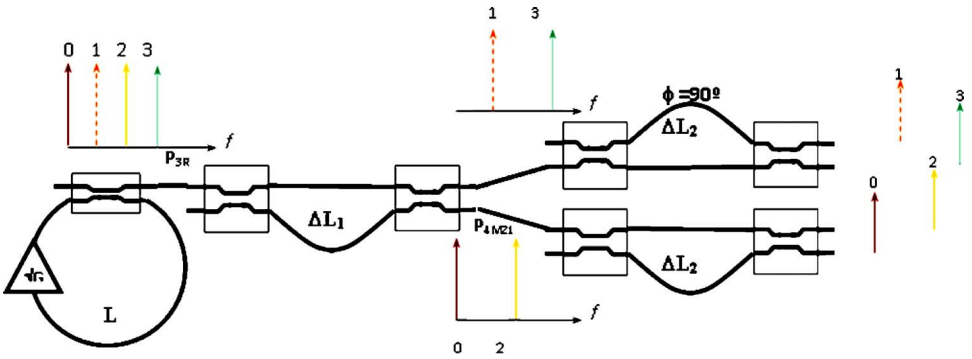

Fig. 22. 1×4 demultiplexer with four equispaced optical carriers.

$$\mathrm{FSR}_T = 2^k \cdot \mathrm{FSR}_{\mathrm{RR}}.$$

An additional constant phase difference should be included in each MZI stage to properly allocate the different channels in frequency. This phase depends on the MZI stage to be considered and is given by

$$\phi = \frac{2\pi N_c}{2^k},$$

where ϕ is the phase introduced in the longer MZI arm, N_c is the number of the first channel at the input of the MZI stage (with the channel $N_c=0$ at the wavelength where both outputs $P_{4\mathrm{MZ1}}$ and $P_{3\mathrm{R}}$ have a peak, without any introduced phase), and k is the number of interferometers in a specific stage (see the example in Fig. 22; there is one interferometer in the first stage, $k=1$, and two interferometers in the second stage, $k=2$, and it is only necessary to introduce an additional $\pi/2$ phase in one of the MZIs of the second stage). The device is made of a RR connected to k cascaded MZI stages.

Tuning Process: RR and MZI output powers are periodic functions, so changing the period of these functions can modify the peak location. The maximum of order N is shifted $N\times\Delta\mathrm{FSR}$ when a change in ΔFSR is forced. This is valid for both the RR and the MZI. This ΔFSR can be forced by changing the lengths L and ΔL through thermal heating or by using a piezoelectric. Another approach is changing the refractive index by thermal heating or with a current injection. Now we are going to describe the tuning process in two steps, first by changing the length and second by modifying the refractive index.

A practical 1×4 2.5 GHz demultiplexer is designed. Channel spacing is determined by the ΔL_{MZ} of the last stage; it is ΔL_2 in this specific design. Thus $\mathrm{FSR}_T=\mathrm{FSR}_{\mathrm{MZ2}}=2\mathrm{FSR}_{\mathrm{MZ1}}=4\mathrm{FSR}_{\mathrm{RR}}$. In our design, the final device has a net gain of 10 dB; using a RR loop gain of 1.56, $K_i=0.5$, and $\gamma_i=0.05$ for every directional coupler in the device, $\alpha=0.001$ neper/m. RR parameters are chosen for having a stable operation with as little dependence on parameter fluctuations as possible [25]. Simulations show a net gain of 10 dB, cross talk greater than –40 dB, and a FWHM of 128.5 MHz. Thus it has gain and high isolation at the expense of a nonflattop passband. But this is not a limitation when it is used in the reception stage. The device is centered on the ITU wavelength grid, 196 THz at channel 0 (see Fig. 22). Proper operation of the active device requires temperature stabilization, which can be achieved using additional control electronics. RR introduces a nonconstant dispersion, which must be evaluated in every design.

A tolerance analysis is carried out to determine the effect of the different parameter (G, K_i, γ_i for every coupler) variations on the FWHM and cross talk of the device. Global deviations of $\Delta K_i=0.05$ and $\Delta\gamma_i=0.05$ are considered, which are widely covered by integrated multimode interference and fiber-optic couplers. For the worst case, FWHM increases up to 220 MHz, and cross talk is reduced to –23 dB with a net gain of 5.7 dB. Thus, even in the worst case, the figures are still suitable and they can be corrected by controlling the RR loop gain.

Ring resonators have applications, among others, as routers in self-routing frequency division multiple access (SR-FDMA) networks and as filters in DWDM systems with carrier spacing of 50 GHz or less [63]. They have also been used in nonlin-

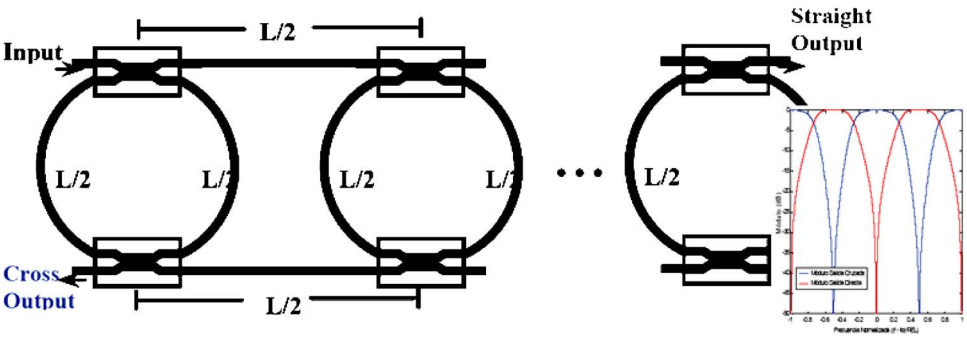

Fig. 23. Add–drop configuration based on cascaded RRs and bandpass flattop response of a fourth-order filter.

ear optical applications such as all-optical switches [64]. The resonant frequencies of filters based on RR devices had already been shifted by changing the equivalent loop length by carrier injection [65] or local heating [63]. Also thermally tunable switches based on ring resonators are reported in [66], and absorption is used for controlling the switch in [67].

More recently microring resonator (μRR) tuning has been achieved by liquid flowing in the microchannel, which constitutes the upper cladding of the resonator waveguides [68], and 3 nm shift by all-optical control using 980 nm light pulses is reported in [69]. On the other hand, liquid crystal (LC) technology has been used as a control element in switching fabrics; it has even demonstrated electrical tuning in ring resonators fabricated from silicon-on-insulator wafers by incorporating nematic liquid crystals as the waveguide side cladding, but achieving a limited tuning range of 0.22 nm [70]. Vertically coupled μRR and cross-grid topology has also been demonstrated; a review of the different achievements can be seen in [71].

RR configuration used as a selective wavelength switch (SWS) in a compound configuration to achieve a flattop passband can be seen in Fig. 23, also referred to as an add–drop configuration. High rejection ratios at each output port can be controlled by the loop gain or coupling coefficient, while tuning of the wavelength is achieved by changing the loop length or effective refractive index, as previously mentioned. Different compound configurations can be used as basic building blocks in filter synthesis techniques; simple RRs are all-pole transfer functions in specific outputs, whereas zeros are introduced by MZ configurations. RRs with Sagnac inside the loop (see Fig. 24) are second-order functions with conjugate poles giving new flexibility to the designs in terms of the number of components, fabrication tolerance, and tunability. Measurements of wavelength selection based on coupling coefficient can be seen in Fig. 24 for a fiber-optic prototype operating under a coherent regime for validating the operation principle [24].

Figure 25 shows a serial 2 μRR in a cross-grid configuration that has been tested as a reconfigurable three-channel demultiplexer. It is a compact 100 μm^2 device on a silicon-on-insulator substrate with nematic liquid crystals having a 28 nm FSR and a 5 nm tuning range, and optimum evanescent coupling lengths are used for improving

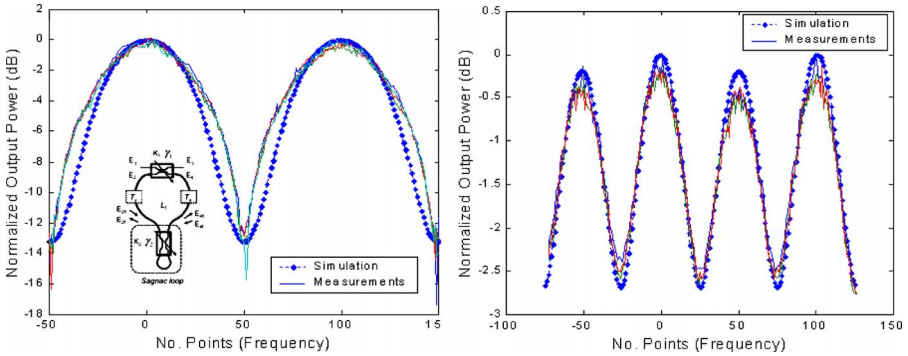

Fig. 24. Measurements and simulations of normalized output power at straight output port versus frequency for K_1=0.92, loss=0.5, K_2=0.75, and K_2=0.505 (in compound configuration shown in the inset).

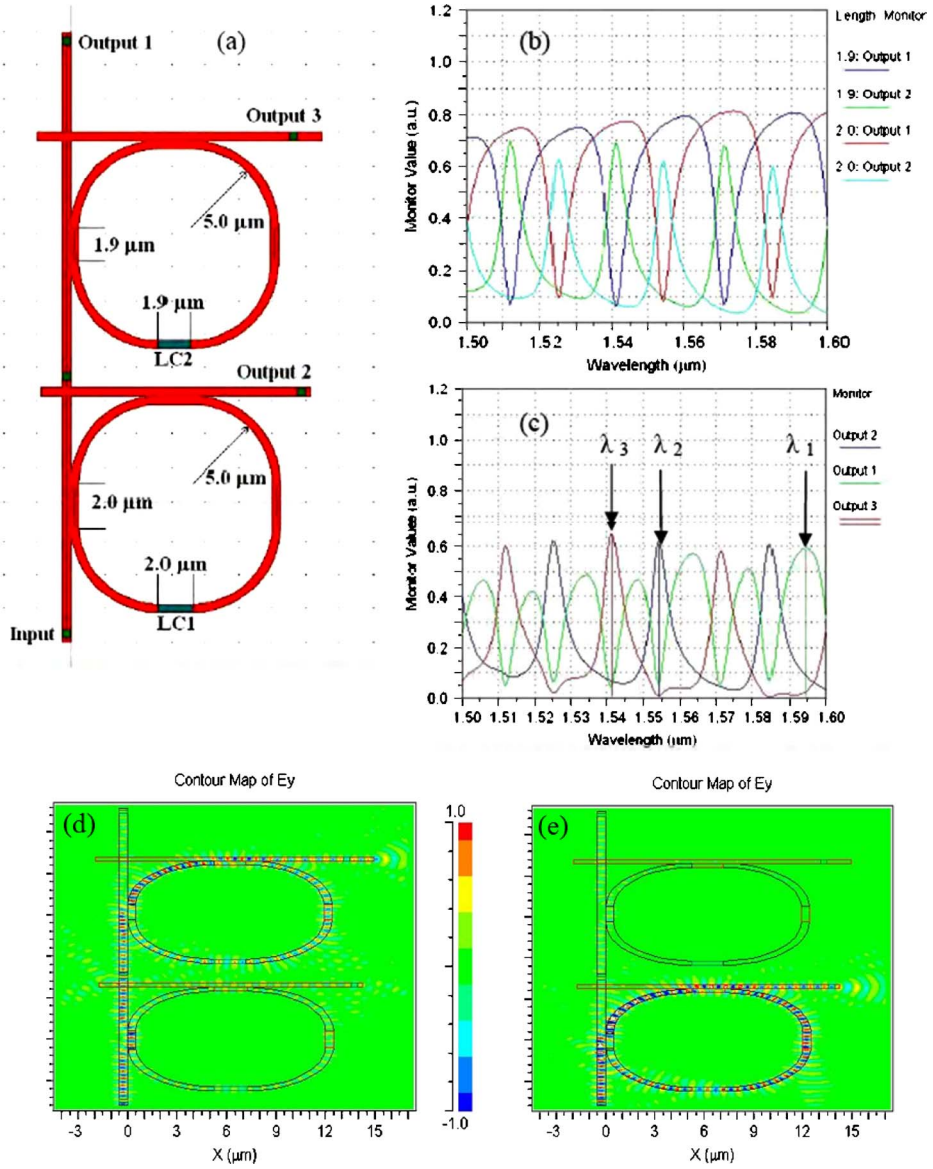

Fig. 25. (a) Serial 2 μRR in a cross-grid configuration; (b) simulations of both single μRR through (output 1) and drop (output 2) versus wavelength, with LC1 (2 μm) and LC2 (1.9 μm), both in the OFF state; (c) compound μRR response and selected channel wavelength at each output port: (1) $\lambda_1 = 1.595$ μm, (2) $\lambda_2 = 1.554$ μm, and (3) $\lambda_3 = 1.541$ μm. Instantaneous electric field intensity for two wavelengths, LC OFF: (d) output 2 maximum, output 1 and 3 minimum for $\lambda = 1.554$ μm and (e) output 3 maximum, output 1 and 2 minimum for $\lambda = 1.595$ μm.

cross-talk and insertion losses. The through (output 1) and drop (output 2) port response versus wavelength for each individual μRR can be seen in Fig. 25(b); they are identified by LC length labels as LC1 (2 μm) and LC2 (1.9 μm), and in all cases the LCs are OFF. Two output power channels versus wavelength in the compound configuration can be seen in Fig. 25(c), where wavelengths that have a maximum output power only at a single output channel have been selected. Instantaneous electric field intensity patterns in the serial μRR configuration are numerically simulated using the commercial software FULLWAVE for the selected input channel wavelengths marked in Fig. 25(c). Results can be seen in Figs. 25(d) and 25(e) for all LCs in the OFF state. It can be seen that the maximum cross talk is achieved for a wavelength of $\lambda = 1.554$ μm demultiplexed at output port 2.

6. Conclusions

In this paper, photonic enabling technologies for implementing an optical router have been reviewed, and further recent advances in critical integration processes, devices,

and subsystems were presented. Key optical subsystems include wavelength converters, exhibiting multidisciplinary applications, ring resonators for implementing advanced photonic multiplexers/demultiplexers, as well as optical logic and packet processing circuits (logic gates, flip-flops, clock/data recovery, etc.). The integration and miniaturization of these devices/circuits is the next big step that will carve the way for their wide deployment and integration in an all-photonic system.

Acknowledgments

The work described in this paper was carried out with the support of the e-Photon/ONe+ and its successor BONE (Building the Future Optical Network in Europe) project, a Network of Excellence funded by the European Commission through the 7th ICT-Framework Programme.

References and Links

1. R. Ramaswami and K. Sivarajan, *Optical Networks: a Practical Perspective* (Morgan Kaufmann, 1998).
2. M. Renaud, F. Masetti, C. Guillemot, and B. Bostica, "Network and system concepts for optical packet switching," IEEE Commun. Mag. **35**(4), 96–102 (1997).
3. K. Vlachos, N. Pleros, C. Bintjas, G. Theophilopoulos, and H. Avramopoulos, "Ultrafast time-domain technology and its application in all-optical signal processing," J. Lightwave Technol. **21**, 1857–1868 (2003).
4. C. Qiao and M. Yoo, "Optical burst switching (OBS)—a new paradigm for an optical Internet," J. High Speed Netw. **8**, 69–84 (1999).
5. D. J. Blumenthal, B.-E. Olsson, G. Rossi, T. E. Dimmick, L. Rau, M. Mašanović, O. Lavrova, R. Doshi, O. Jerphagnon, J. E. Bowers, V. Kaman, L. A. Coldren, and J. Barton, "All-optical label swapping networks and technologies," J. Lightwave Technol. **18**, 2058–2075 (2000).
6. H. J. Chao, M. Degermark, N. McKeown, and H. H.-Y. Tzeng, "Next-generation IP switches and routers," IEEE J. Sel. Areas Commun. **17**, 1009–1012 (1999).
7. S. J. B. Yoo, F. Xue, Y. Bansal, J. Taylor, Z. Pan, J. Cao, M. Jean, T. Nady, G. Goncher, K. Boyer, K. Okamoto, S. Kamei, and V. Akella, "High-performance optical-label switching packet routers and smart edge routers for the next-generation Internet," IEEE J. Sel. Areas Commun. **21**, 1041–1051 (2003).
8. http://www.e-photon-one.org/ephotonplus.
9. http://www.ict-bone.eu/.
10. C. Raffaelli, K. Vlachos, N. Andriolli, D. Apostolopoulos, J. Buron, R. van Caenegem, G. Danilewicz, J. M. Finochietto, J. Garcia-Haro, D. Klanidis, M. O'Mahoney, G. Maier, A. Pattavina, P. Pavon-Marino, S. Ruepp, M. Savi, M. Scaffardi, I. Tomkos, A. Tzanakaki, L. Wosinska, O. Zouraraki, and F. Neri, "Photonics in switching: architectures, systems and enabling technologies," Comput. Netw. **52**, 1873–1890 (2008).
11. Y. Liu, E. Tangdiongga, M. T. Hill, J. H. C. van Zantvoort, J. H. den Besten, T. de Vries, E. Smalbrugge, Y.-S. Oei, X. J. M. Leijtens, M. K. Smit, A. M. J. Koonen, G. D. Khoe, and H. J. S. Dorren, "Ultrafast all-optical wavelength routing of data packets utilizing an SOA-based wavelength converter and a monolithically integrated optical flip-flop," IEEE J. Sel. Top. Quantum Electron. **14**, 801–807 (2008).
12. S. A. Hamilton, B. S. Robinson, T. E. Murphy, S. J. Savage, and E. P. Ippen, "100 Gb/s optical time-division multiplexed networks," J. Lightwave Technol. **20**, 2086–2100 (2002).
13. G. Maxwell, B. Manning, M. Nield, M. Hariow, C. Ford, M. Clements, S. Lucas, P. Townley, R. McDougall, S. Oliver, R. Cecil, L. Johnston, A. Poustie, R. Webb, I. Lealman, L. Rivers, J. King, S. Perrin, R. Moore, I. Reid, and D. Scrase, "Very low coupling loss, hybrid-integrated all-optical regenerator with passive assembly," in *28th European Conference on Optical Communication* (IEEE, 2002), paper PD3.5.
14. M. Masanovic, V. Lal, J. S. Barton, E. J. Skogen, L. A. Coldren, and D. J. Blumenthal, "Monolithically integrated Mach–Zehnder interferometer wavelength converter and widely tunable laser in InP," IEEE Photon. Technol. Lett. **15**, 1117–1119 (2003).
15. J. Leuthold, L. Möller, J. Jaques, S. Cabot, L. Zhang, P. Bernasconci, M. Cappuzzo, L. Gomez, E. Laskowski, E. Chen, A. Wong-Foy, and A. Griffin, "160 Gb/s SOA all-optical wavelength converter and assessment of its regenerative properties," in *Optical Amplifiers and Their Applications/Integrated Photonics Research*, Technical Digest (CD) (Optical Society of America, 2004), paper OTuB2.
16. http://www.ciphotonics.com.
17. G. Maxwell, R. McDougall, R. Harmon, M. Nield, L. Rivers, A. Poustie, F. Gunning, M. Yang, A. D. Ellis, R. Webb, and R. Manning, "WDM-enabled, 40 Gb/s hybrid integrated all-optical regenerator," in *31st European Conference on Optical Communication*, Vol. 6 (IEEE, 2005) postdeadline paper, pp. 15–16.
18. G. Rossi, O. Jerphagnon, B. Olsson, and D. J. Blumenthal, "Optical SCM data extraction using a fiber-loop mirror for WDM network systems," IEEE Photon. Technol. Lett. **12**, 897–899 (2000).
19. D. Sadot and E. Boimovich, "Tunable optical filters for dense WDM networks," IEEE Commun. Mag. **36**(12), 50–55 (1998).

20. B. E. Little, S. T. Chu, P. P. Absil, J. V. Hryniewicz, F. G. Johnson, F. Seiferth, D. Gill, V. Van, O. Ing, and M. Trakalo, "Very high-order microring resonator filters for WDM applications," IEEE Photon. Technol. Lett. **16**, 2263–2265 (2004).
21. J. E. Heebner, P. Chak, S. Pereira, J. E. Sipe, and R. W. Boyd, "Distributed and localized feedback in microresonator sequences for linear and nonlinear optics," J. Opt. Soc. Am. B **21**, 1818–1832 (2004).
22. O. Schwelb and I. Frigyes, "All-optical tunable filters built with discontinuity-assisted ring resonators," J. Lightwave Technol. **19**, 4–386 (2001).
23. S. Vargas, C. Vázquez, and J. M. S. Pena, "Wide tunable filters using a recirculating delay line with multi-reflections," Opt. Eng. (Bellingham) **41**, 926–927 (2002).
24. C. Vázquez, S. Vargas, J. M. S. Pena, and P. Corredera, "Tunable optical filters using compound ring resonators for DWDM," IEEE Photon. Technol. Lett. **15**, 1085–1087 (2003).
25. C. Vázquez, S. Vargas, and J. M. S. Pena, "Design and tolerance analysis of a router using an amplified ring resonator and Bragg gratings," Appl. Opt. **39**, 1934–1940 (2000).
26. M. M. Lee and M. C. Wu, "A MEMS-actuated tunable microdisk resonator," in *IEEE/LEOS International Conference on Optical MEMS* (IEEE, 2003), paper MC3.
27. W. M. J. Green, R. K. Lee, A. Yariv, and M. A. Scherer, "Control of optical waveguide-resonator coupling: application to low-power optical modulation and switching," in *The 16th Annual Meeting of the IEEE Lasers and Electro-Optics Society* (IEEE, 2003), paper MM3, pp. 130–131.
28. K. Stubkjaer, "Semiconductor optical amplifier-based all-optical gates for high-speed optical processing," IEEE J. Sel. Top. Quantum Electron. **6**, 1428–1435 (2000).
29. I. White, R. Penty, M. Webster, J. C. Yew, A. Wonfor, and S. Shahkooh, "Wavelength switching components for future photonic networks," IEEE Commun. Mag. **40**(9), 74–81 (2002).
30. A. D. Ellis, A. E. Kelly, D. Nesset, R. Kashyap, and D. G. Moody, "Error free 100 Gbit/s wavelength conversion using grating assisted cross gain modulation in 2 mm long semiconductor amplifier," Electron. Lett. **34**, 1958–1959 (1998).
31. Y. Liu, E. Tangdiongga, Z. Li, H. de Waardt, A. M. J. Koonen, G. D. Khoe, X. Shu, I. Bennion, and H. J. S. Dorren, "Error-free 320 Gb/s all-optical wavelength conversion using a single semiconductor optical amplifier," J. Lightwave Technol. **25**, 103–108 (2007).
32. S. Nakamura, Y. Ueno, and K. Tajima, "168-Gb/s all-optical wavelength conversion with a symmetric-Mach–Zehnder-type switch," IEEE Photon. Technol. Lett. **13**, 1091–1093 (2001).
33. B. Mikkelsen, T. Durhuus, C. Joergensen, R. J. S. Pederson, S. L. Danielsen, and K. E. Stubkjaer, "10 Gbit/s wavelength converter realised by monolithic integration of semiconductor optical amplifiers and Michelson inteferometer," in *Proceedings of ECOC'94* (IEEE, 1994), Vol. 4, pp. 67–70.
34. T. Durhuus, C. Joergensen, B. Mikkelsen, R. J. S. Pedersen, and K. E. Stubkjaer, "All optical wavelength conversion by SOA's in a Mach–Zehnder configuration," IEEE Photon. Technol. Lett. **6**, 53–55 (1994).
35. J. Yu, X. Zheng, C. Peucheret, A. T. Clausen, H. N. Poulsen, and P. Jeppesen, "40 Gb/s all-optical wavelength conversion based on a nonlinear optical loop mirror," J. Lightwave Technol. **18**, 1001–1010 (2000).
36. B.-E. Olsson, P. Ohlen, L. Rau, and D. J. Blumenthal, "A simple and robust 40-Gb/s wavelength converter using fiber cross-phase modulation and optical filtering," IEEE Photon. Technol. Lett. **12**, 846–848 (2002).
37. T. Yamamoto, E. Yoshida, and M. Nakazawa, "Ultrafast nonlinear optical loop mirror for demultiplexing 640 Gbit/s TDM signals," Electron. Lett. **34**, 1013–1014 (1998).
38. S. Diez, C. Schmidt, R. Ludwig, H. G. Weber, K. Obermann, S. Kindt, I. Koltchanov, and K. Petermann, "Four wave mixing in semiconductor optical amplifiers for frequency conversion and fast optical switching," IEEE J. Sel. Top. Quantum Electron. **3**, 1131–1145 (1997).
39. D. F. Geraghty, R. B. Lee, M. Verdiell, M. Ziari, A. Mathur, and K. J. Vahala, "Wavelength conversion for WDM communication systems using four wave mixing in semiconductor optical amplifiers," IEEE J. Sel. Top. Quantum Electron. **3**, 1146–1157 (1997).
40. A. Hsu and S. L. Chuang, "Wavelength conversion by dual-pump four-wave mixing in an integrated laser modulator," IEEE Photon. Technol. Lett. **15**, 1120–1122 (2003).
41. M. Sugawara, H. Ebe, N. Hatori, M. Ishida, Y. Arakawa, T. Akiyama, K. Otsubo, and Y. Nakata, "Theory of optical signal amplification and processing by quantum-dot semiconductor optical amplifiers," Phys. Rev. B **69**, 235332 (2004).
42. W. Wang, L. G. Rau, and D. J. Blumenthal, "160 Gb/s variable length packet/10 Gb/s-label all-optical label switching with wavelength conversion and unicast/multicast operation," J. Lightwave Technol. **23**, 211–218 (2005).
43. M. Scaffardi, F. Fresi, A. Bogoni, and L. Potì, "Implementation of a tunable 160 Gb/s wavelength multi-converter based on supercontinuum in a highly nonlinear fibre," in *Proceedings of ECOC 2006* (IEEE, 2006), paper Th3.5.4.
44. T. Akiyama, M. Sugawara, and Y. Arakawa, "Quantum-dot semiconductor optical amplifiers," Proc. IEEE **95**, 1757–1766 (2007).
45. M. Spyropoulou, S. Sygletos, and I. Tomkos, "Simulation of multiwavelength regeneration based on QD semiconductor optical amplifiers," IEEE Photon. Technol. Lett. **19**, 1577–1579 (2007).
46. M. Sugawara, T. Akiyama, N. Hatori, Y. Nakata, H. Ebe, and H. Ishikawa, "Quantum-dot semiconductor optical amplifiers for high-bit-rate signal processing up to 160 Gb/s and a new scheme of 3R regenerators," Meas. Sci. Technol. **13**, 1683–1691 (2002).

47. D. K. Hunter, M. C. Chia, and I. Andonovic, "Buffering in optical packet switches," J. Lightwave Technol. **16**, 2081–2094 (1998).
48. D. Apostolopoulos, D. Petrantonakis, O. Zouraraki, E. Kehayas, N. Pleros, and H. Avramopoulos, "All-optical label/payload separation at 40 Gb/s," IEEE Photon. Technol. Lett. **18**, 2023–2026 (2006).
49. D. Tsiokos, P. Bakopoulos, A. Poustie, G. Maxwell, and H. Avramopoulos, "Jitter reduction in a 40 Gb/s all-optical 3R regenerator using integrated MZI-SOA switches," Electron. Lett. **42**, 817–819 (2006).
50. R. S. Tucker, "The role of optics and electronics in high-capacity routers," J. Lightwave Technol. **24**, 4655–4673 (2006).
51. M. C. Chia, D. K. Hunter, I. Andonovic, P. Ball, I. Wright, S. P. Ferguson, K. M. Guild, and M. J. O'Mahoney, "Packet loss and delay performance of feedback and feed-forward arrayed-waveguide gratings-based optical packet switches with WDM inputs-outputs," J. Lightwave Technol. **19**, 1241–1254 (2001).
52. C. M. Gauger, "Dimensioning of FDL buffers for optical burst switching nodes," in *Proceedings of the 6th IFIP Working Conference on Optical Network Design and Modeling (ONDM 2002)* (IFIP, 2002), pp. 117–132.
53. E. F. Burmeister and J. E. Bowers, "Integrated gate matrix switch for optical packet buffering," IEEE Photon. Technol. Lett. **18**, 103–105 (2006).
54. R. S. Tucker, P.-C. Ku, and C. J. Chang-Hasnain, "Slow-light optical buffers: capabilities and fundamental limitations," J. Lightwave Technol. **23**, 4046–4066 (2005).
55. H. Kawaguchi, "All-optical signal regeneration and optical buffering using polarization bistable VCSELs," in *International Conference on Transparent Optical Networks* (IEEE, 2006), pp. 24–27.
56. H.-D. Jung, I. T. Monroy, A. M. J. Koonen, and E. Tangdiongga, "All-optical data vortex node using an MZI-SOA switch array," IEEE Photon. Technol. Lett. **19**, 1777–1779 (2007).
57. O. Zouraraki, K. Yiannopoulos, P. Zakynthinos, D. Petrantonakis, E. Varvarigos, A. Poustie, G. Maxwell, and H. Avramopoulos, "Optical packet buffering in all-optical time-slot-interchanger architecture," IEEE Photon. Technol. Lett. **19**, 1307–1309 (2007).
58. K. Yiannopoulos, K. Vlachos, and E. Varvarigos, "Multiple-input buffer and shared buffer architectures for optical packet and burst switching networks," J. Lightwave Technol. **25**, 1379–1389 (2007).
59. M. Takenaka, M. Raburn, and Y. Nakano, "All-optical flip-flop multimode interference bistable laser diode," IEEE Photon. Technol. Lett. **17**, 968–970 (2005).
60. H. Kawaguchi, I. S. Hidayat, Y. Takahashi, and Y. Yamayoshi, "Pitchfork bifurcation polarisation bistability in vertical-cavity surface-emitting lasers," Electron. Lett. **31**, 109–111 (1995).
61. Y. Liu, M. T. Hill, N. Calabretta, H. De Waardt, G. D. Khoe, and H. J. S. Dorren, "Tree-state all-optical memory based on coupled ring lasers," IEEE Photon. Technol. Lett. **15**, 1461–1463 (2003).
62. A. Malacarne, A. Bogoni, and L. Potì, "An optical flip-flop based on erbium-ytterbium doped fibre," in *Proceedings of ECOC 2006* (IEEE, 2006), paper We3, p. 31.
63. B. E. Little, S. T. Chu, P. P. Absil, J. V. Hryniewicz, F. G. Johnson, F. Seiferth, D. Gill, V. Van, O. King, and M. Trakalo, "Very high-order microring resonator filters for WDM applications," IEEE Photon. Technol. Lett. **16**, 2263–2265 (2004).
64. J. E. Heebner and R. W. Boyd, "Enhanced all-optical switching by use of a nonlinear fiber ring resonator," Opt. Lett. **24**, 847–849 (1999).
65. K. Djordjev, S. Choi, S. Chou, and P. Dapkus, "Microdisk tunable resonant filters and switches," IEEE Photon. Technol. Lett. **14**, 828–830 (2002).
66. K. Djordjev, S. Choi, S. Chou, and P. Dapkus, "Vertically coupled InP microdisk switches devices with electroabsorptive active regions," IEEE Photon. Technol. Lett. **14**, 1115–1117 (2002).
67. D. H. Geusebroek, E. J. Klein, H. Kelderman, F. S. Tan, D. J. W. Klunder, and A. Driessen, "Thermally tunable, wide FSR switch based on micro-ring resonators," in *Proceedings of the Symposium IEEE/LEOS Benelux Chapter* (IEEE, 2002), pp. 155–158.
68. U. L. K. Campbell, A. Groisman, S. Mookherjea, and Y. Fainman, "On-chip microfluidic tuning of an optical microring resonator," Appl. Phys. Lett. **88**, 111107 (2006).
69. M. Beaugeois, B. Pinchemel, and M. Bouazaoui, M. Lesecq, S. Maricot, and J. P. Vilcot, "All-optical tunability of InGaAsP/InP microdisk resonator by infrared light irradiation," Opt. Lett. **32**, 35–37 (2007).
70. B. Maune, R. Lawson, C. Gunn, A. Scherer, and L. Dalton, "Electrically tunable ring resonators incorporating nematic liquid crystals as cladding layers," Appl. Phys. Lett. **83**, 4689–4691 (2003).
71. K. Tada, T. Suhara, K. Kikuchi, Y. Kokubun, K. Utaka, M. Asada, F. Koyama, and T. Arakawa, *Photonics Based on Wavelength Integration and Manipulation* (The Institute of Pure and Applied Physics, 2005), pp. 303–316.